

Title: Alteration of magmatic monazite in granitoids from the Ryoke belt (SW Japan): processes and consequences
Manuscript Number: 7025R - CORRECTION
Authors: Etienne Skrzypek, University of Graz Shuhei Sakata, Gakushuin University Dominik Sorger, University of Graz

1 **Alteration of magmatic monazite in granitoids from the Ryoke belt (SW Japan):**
2 **processes and consequences**

3

4 **REVISION 1**

5 **Corrected October 31st 2019**

6

7 **ETIENNE SKRZYPEK^{1,2*}, SHUHEI SAKATA³ AND DOMINIK SORGER²**

8 ¹Department of Geology and Mineralogy, Graduate School of Science, Kyoto University,
9 Kitashirakawa-Oiwakecho, Sakyo-ku, Kyoto 606-8502, Japan

10 ²Department of Petrology and Geochemistry, NAWI Graz Geocenter, University of Graz,
11 Universitätsplatz 2, 8010 Graz, Austria

12 ³Department of Chemistry, Faculty of Science, Gakushuin University, 1-5-1 Mejiro, Toshima-
13 ku, Tokyo 171-8588, Japan

14 * E-mail: etienne.skrzypek@uni-graz.at

15

16 **Running title:** Alteration of magmatic monazite

17

18 With 7 figures and 2 tables

19

20 **ABSTRACT**

21 The alteration of magmatic monazite and its consequences for monazite geochronology are
22 explored in granitoids from the western part of the Ryoke belt (Iwakuni-Yanai area, SW
23 Japan). Biotite-granite samples were collected in two plutons emplaced slightly before the
24 main tectono-metamorphic event: one, a massive granite (Shimokuhara) adjoins schistose
25 rocks affected by greenschist facies metamorphism; and the second, a gneissose granite
26 (Namera) adjoins migmatitic gneiss that experienced upper-amphibolite facies conditions.
27 Despite contrasting textures, the granite samples have similar mineral modes and
28 compositions. Monazite in the massive granite is dominated by primary domains with limited
29 secondary recrystallization along cracks and veinlets. It is variably replaced by
30 allanite+apatite±xenotime±Th–U-rich phases. The outermost rims of primary domains yield a
31 weighted average $^{206}\text{Pb}/^{238}\text{U}$ date of 102 ± 2 Ma while the Th–U phases show Th–U–Pb dates
32 of 58 ± 5 and $15\text{--}14 \pm 2\text{--}3$ Ma. Monazite in the gneissose granite preserves sector- or
33 oscillatory-zoned primary domains cross-cut by secondary domains enriched in Ca, Y, U, P
34 and containing numerous inclusions. The secondary domains preserve concordant $^{206}\text{Pb}/^{238}\text{U}$
35 dates spreading from 102 ± 3 to 91 ± 2 Ma while primary domain analyses are commonly
36 discordant and range from 116 to 101 Ma.

37 Monazite alteration textures in the two granites chiefly reflect differences in their post-
38 magmatic histories. In the massive granite, monazite replacement occurred via a nearly
39 stoichiometrically-balanced reaction reflecting interaction with an aqueous fluid enriched in
40 Ca+Al+Si±F during hydrothermal alteration of the granitic assemblage, likely below 500 °C.
41 In the gneissose granite a small amount of anatectic melt, probably derived from the
42 neighboring metasedimentary rocks, was responsible for a pseudomorphic recrystallization of
43 monazite by dissolution-reprecipitation above 600 °C. Regardless of whether monazite
44 underwent replacement or recrystallization, primary monazite domains preserve the age of

45 magmatic crystallization for both plutons (102 ± 2 Ma and 106 ± 5 Ma). Conversely, the age
46 of monazite alteration is not easily resolved. Monazite replacement in the massive granite
47 might be constrained using the Th–U-rich alteration products; with due caution and despite
48 probable radiogenic Pb loss, the oldest date of 58 ± 5 Ma could be ascribed to chloritization
49 during final exhumation of the granite. The spread in apparently concordant $^{206}\text{Pb}/^{238}\text{U}$ dates
50 for secondary domains in the gneissose granite is attributed to incomplete isotopic resetting
51 during dissolution-reprecipitation, and the youngest date of 91 ± 2 Ma is considered as the age
52 of monazite recrystallization during a suprasolidus metamorphic event. These results reveal a
53 diachronous, ca. 10 Ma-long HT history and an overall duration of about 15 Ma for the
54 metamorphic evolution of the western part of the Ryoke belt.

55

56 **Keywords:** Monazite replacement, monazite recrystallization, dissolution-reprecipitation,
57 partial melting, LA-ICP-MS geochronology, Ryoke plutono-metamorphic belt

58 **INTRODUCTION**

59 Monazite, a lanthanide- and actinide-bearing phosphate, is a valuable petrological and
60 geochronological tool. In metamorphic rocks, it can be used to decipher the age and
61 Pressure–Temperature (P – T) conditions of distinct orogenic events (e.g. Williams et al. 1999;
62 Foster et al. 2004; Engi 2017) while in magmatic rocks it is useful for dating pluton
63 emplacement (e.g. Harrison et al. 1995; Be Mezeme et al. 2006), especially in cases where
64 zircon dates appear unreliable (Kusiak et al. 2004; Piechocka et al. 2017). However, monazite
65 is also known to be a versatile mineral (e.g. Catlos, 2013), so its petrochronological potential
66 must be carefully assessed.

67 In granitoids from the Ryoke belt (SW Japan), age dating of different samples from
68 the same pluton revealed a discrepancy between magmatic zircon and monazite dates. There
69 are cases of $^{206}\text{Pb}/^{238}\text{U}$ zircon dates being older than Th–U–Pb monazite dates (Skrzypek et al.
70 2016), and vice versa (Takatsuka et al. 2018a, b). When monazite dates are younger than
71 zircon's, it is commonly suspected that monazite reacted during post-magmatic processes, as
72 the mineral is prone to fluid-induced compositional modifications and/or age resetting (e.g.
73 Kelly et al. 2012; Seydoux-Guillaume et al. 2012; Villa and Williams 2013; Taylor et al.
74 2014). Thus, our objective was to identify monazite alteration textures and document possible
75 age discrepancies when zircon and monazite from the same sample are dated with the same
76 method.

77 The monazite-bearing granitoid samples described by Skrzypek et al. (2016) for zircon
78 dating (Iwakuni-Yanai area, western part of the Ryoke belt) represent a suitable material, as
79 they contain monazite with common alteration textures and different age populations. In this
80 contribution we document in detail the post-magmatic monazite alteration textures and
81 evaluate their impact on monazite's geochronological record. We focus on two granite
82 samples that have (1) crystallization ages slightly older (~5 Ma) than the main (regional)

83 tectono-metamorphic event recorded in the neighboring metasedimentary rocks, (2) similar
84 whole-rock compositions, and (3) contrasting monazite textures. The massive Shimokuhara
85 granite lies next to schistose rocks where regional conditions did not exceed ~2.5 kbar/550 °C
86 (Ikeda 2004), whereas the gneissose Namera granite adjoins migmatitic gneissose rocks where
87 regional metamorphism reached ~3 kbar/675 °C (Ikeda 2004; Fig. 1). As such, these two
88 granites provide an opportunity to explore the response of magmatic monazite to post-
89 emplacement metamorphism of varying grade. First, we report the mineralogy, texture and
90 mineral mode of biotite-granite samples from both plutons to assess their degree of similarity.
91 We then document their monazite textures, and date monazite *in situ* by laser ablation
92 inductively-coupled mass spectrometry (LA-ICP-MS). The results are used to identify the
93 processes involved in the alteration of magmatic monazite and the consequences for age
94 dating of magmatic/metamorphic events.

95 **BACKGROUND: ALTERATION OF MAGMATIC MONAZITE**

96 The alteration of magmatic monazite follows two mechanisms: *replacement* by other phases
97 and/or *recrystallization* of new monazite. The most commonly observed monazite
98 replacement texture in (meta-)igneous rocks involves the peripheral growth of allanite, apatite
99 and minor Th–U-bearing phases following a nearly balanced reaction (e.g. Murata et al. 1957;
100 Broska and Siman 1998). Interestingly, monazite replacement by allanite and/or apatite is
101 reported in granitoids that underwent no metamorphism (Broska et al. 2005), greenschist
102 facies hydrothermal alteration (~340 °C; Ward et al. 1992; Poitrasson et al. 2000), and lower-
103 (5–6 kbar/550–600°C; Finger et al. 1998) to upper-amphibolite facies metamorphism (4–8
104 kbar/685–825°C; Broska et al. 2005). An extreme example of monazite replacement by
105 Aln–Ap at the magmatic stage is attributed to an increase in the Ca content of the melt (Dini
106 et al. 2004). Other cases of monazite replacement at low temperature (290–350 °C) involve

107 the growth of pyrite + brockite (Poitrasson et al. 2000) or thorite + fluorapatite + synchysite
108 (Didier et al. 2013) assemblages.

109 Monazite recrystallization corresponds to the formation of new domains with a
110 composition that differs from the initial magmatic grain. In this case a balanced reaction is
111 difficult to infer and it is only possible to document the relative element enrichment/depletion
112 with respect to primary monazite. Recrystallization may result in monazite evolving towards a
113 cheralitic [$\text{Ca}_{0.5}\text{Th}_{0.5}\text{PO}_4$], huttonitic [ThSiO_4], Heavy REE (HREE)-richer or U-rich
114 composition (Jefferies 1985; Ward et al. 1992; Poitrasson et al. 1996; 2000; Townsend et al.
115 2000; Didier et al. 2013). Again, monazite recrystallization is observed across a wide range of
116 P - T conditions; it is ascribed to relatively low- T chloritization or greisenization (Jefferies
117 1985; Ward et al. 1992; Poitrasson et al. 1996; 2000; Didier et al. 2013) and high- T , late- to
118 post-magmatic fluid-mineral interaction (Hawkins and Bowring 1997). There is no evident
119 link between P - T conditions and the composition of newly-formed monazite, but the extent
120 of recrystallization seems to increase with metamorphic grade. Townsend et al. (2000)
121 observed that monazite recrystallization occurs along micron-scale veins in low-grade
122 samples (~ 1.5 kbar/ < 350 – 400 °C), whereas larger patchy domains are formed at higher grade
123 (~ 3 – 4 kbar/ 400 – 700 °C).

124 **GEOLOGICAL OUTLINE**

125 The Ryoke belt is an association of Cretaceous plutonic and metamorphic rocks located in SW
126 Japan (e.g. Nakajima 1994). The Iwakuni-Yanai area (W part of the Ryoke belt) exposes Late
127 Jurassic accretionary-wedge sediments metamorphosed along a low- P /high- T gradient and
128 intruded by abundant granitoids (Fig. 1; e.g. Brown 1998). From north to south, the weakly-
129 metamorphosed sediments transition to a low-grade schist zone and then a high-grade gneiss
130 zone (Fig. 1; Higashimoto et al. 1983). The tectono-metamorphic history involves an initial
131 contact metamorphic event followed by the growth of syn-tectonic parageneses that are used

132 to define the E–W trending, so-called regional metamorphic zones (Fig. 1; Ikeda 1998;
133 Okudaira et al. 2001; Skrzypek et al. 2016).

134 For metamorphic rocks, U–Pb zircon dating in the highest-grade Grt–Crd zone
135 brackets the timing of suprasolidus conditions between 103 and 97 Ma (Nakajima et al. 2013;
136 Skrzypek et al. 2016). Metamorphic monazite in the Kfs–Crd and Grt–Crd zones shows
137 features that indicate growth at mainly prograde to peak temperature conditions (600–800
138 °C), but U–Pb monazite dates ranging from ca. 100 down to 85 Ma are obtained, so that the
139 persistence of medium-*T* conditions (> 200–300 °C) until 85 Ma was proposed (Skrzypek et
140 al. 2018). U–Pb zircon ages for granitoids, in agreement with structural and petrological
141 observations, indicate pluton intrusion before (105–100 Ma), during (~100 Ma) and after (~96
142 Ma) the regional metamorphic peak (Fig. 1; Herzig et al. 1998; Nakajima et al. 2013;
143 Skrzypek et al. 2016). The present study focuses on the granitoids (Shimokuhara and Namera)
144 emplaced in the sediments before the metamorphic peak, and therefore affected by subsequent
145 regional metamorphism.

146 The Shimokuhara granite abuts schistose rocks of the Bt and Ms–Crd metamorphic
147 zones (Fig. 1). It is a massive, biotite-bearing granite that commonly shows biotite
148 chloritization, and locally contains K-feldspar phenocrysts, garnet, tourmaline and allanite as
149 primary phases (Murakami 1970; Higashimoto et al. 1983; Moutte and Iiyama 1984). The
150 contact with metasedimentary rocks gently dips to the east, and a metamorphic aureole
151 defined by andalusite porphyroblasts extends up to ~1 km east of the exposed contact
152 (Skrzypek et al. 2016). The pluton is thought to have intruded at a maximum depth of 2–3 km
153 (Murakami 1970). Peak *P–T* estimates for regional metamorphism in the neighboring
154 schistose rocks range from 1 kbar/450 °C to 2.5 kbar/550 °C (Ikeda 2004). For a biotite-
155 granite sample, U–Pb dating of sector- and oscillatory-zoned zircon by LA-ICP-MS revealed
156 ²⁰⁶Pb/²³⁸U dates ranging from 108 to 102 Ma, with 105 ± 3 Ma being taken as the age of

157 granite intrusion (Skrzypek et al. 2016). Monazite dating of two granite samples by the
158 chemical isochron method (CHIME) yielded 87.3 ± 1.6 and 86.6 ± 2.1 Ma, and these results
159 were also regarded as the age of granite intrusion (Suzuki et al. 1996). K–Ar dating on biotite
160 from a two-mica granodiorite sample gave 87 Ma (data from Kawano and Ueda 1966,
161 recalculated by Higashimoto et al. 1983).

162 The Namera granite lies next to gneissose rocks of the Kfs–Crd zone (Fig. 1). It is
163 mainly a muscovite–biotite-bearing granite with a moderate gneissosity defined by aligned
164 biotite, but it locally shows a granodioritic or leucocratic facies. Accessory garnet and fibrous
165 sillimanite are reported, with pinitized cordierite observed in the leucocratic facies (Nureki
166 1974; Higashimoto et al. 1983). The contact with metasedimentary rocks gently dips towards
167 the east; isolated granite outcrops within the metasedimentary succession (Kfs–Crd zone; not
168 shown in Fig. 1) suggest that the Namera granite extends eastwards and lies a few meters
169 below the metasediments. Peak P – T conditions of regional metamorphism in the neighboring
170 gneissic rocks are estimated at 2–3 kbar/590–675 °C (Ikeda 2004). For a biotite-granite
171 sample, U–Pb dating of oscillatory-zoned zircon by LA-ICP-MS yielded $^{206}\text{Pb}/^{238}\text{U}$ dates
172 between 107 and 100 Ma, with 105 ± 2 Ma being regarded as the age of granite intrusion
173 (Skrzypek et al. 2016). Monazite CHIME dates for three granite samples cluster at 91 – $89.9 \pm$
174 3.2 Ma and are also ascribed to granite intrusion (Suzuki et al. 1996). A K–Ar biotite date of
175 86.6 ± 4.3 Ma was obtained from a hornblende-biotite granite sample (Higashimoto et al.
176 1983).

177 ANALYTICAL METHODS

178 Two samples were collected for each granite and renamed for simplicity. The main samples
179 for the Shimokuhara granite (EY99A, renamed SHK) and Namera granite (EY117A, renamed
180 NAM) are the same as those described by Skrzypek et al. (2016) for U–Pb zircon dating.
181 They are used for both petrological descriptions and monazite geochronology. These samples

182 located close to the pluton margins were selected to explore the effects of post-emplacment
183 metamorphism whose P – T conditions are recorded in the adjacent metamorphic rocks. The
184 additional samples (EY152A, renamed SHK2; EY140A, renamed NAM2) were collected
185 slightly farther from the pluton margin (100–300 m) and are used for comparing monazite
186 textures and compositions. Sample locations are indicated on Figure 1.

187 Mineral compositions were analyzed at Kyoto University and at the University of
188 Graz. In order to use a low beam current (500 pA), chlorite was measured on a scanning
189 electron microscope (Hitachi S3500H, Kyoto) equipped with an energy-dispersive system
190 (EDS) at 20 kV. All other minerals were measured with a JEOL JXA-8105 (Kyoto) and a
191 JEOL JXA-8530F Plus (Graz) electron microprobe (EMP) at 15 kV and with a 3 μ m beam
192 diameter. Analyses of all silicates except Aln were done at 10 nA and corrected with the ZAF
193 method, while those of REE \pm Th \pm U-bearing minerals were done at 150 nA and corrected
194 following the Bence and Albee (1968) method with the updated α -factor table of Kato (2005).
195 The analytical procedure for REE \pm Th \pm U-bearing minerals followed published guidelines (e.g.
196 Scherrer et al. 2000; Pyle et al. 2005; Suzuki and Kato 2008) and is available as Supplemental
197 Material together with the full set of monazite analyses. The REE measured for most
198 monazite analyses are La, Ce, Pr, Nd, Sm and Gd, but several analyses with the additional
199 HREE Tb to Yb were performed for Mnz–Xtm thermometry. Monazite $[A_4(TO_4)_4]$ is
200 described according to A-site (Ca^{2+} , REE $^{3+}$, Y^{3+} , Th^{4+} , U^{4+} , Pb^{2+}) and T-site (P^{5+} , Si^{4+})
201 cations. Its composition is expressed according to the end-members X_{mnz} $[(\Sigma_{REE}+Y)/A]$, X_{cher}
202 $[2Ca/A]$ and X_{hut} $[(Th+U+Pb-Ca)/A]$, where A represents the sum of A-site cations. For
203 Mnz–Xtm thermometry, $X_{(HREE,Y)}$ in monazite is defined as $[(\Sigma_{HREE}+Y)/A]$, with Σ_{HREE}
204 including elements from Gd to Yb. For EMP age dating of the Th–U phases, the accuracy was
205 checked with several analyses of “ekinite” from Okkampitiya, Sri Lanka ($^{207}Pb/^{206}Pb$

206 age = 562.1 ± 0.8 Ma; Nasdala et al. 2017) that yielded a weighted average Th–U–Pb age of
207 564 ± 6 Ma (n=5; MSWD=0.15).

208 Several calibrations are available for Mnz–Xtm thermometry. While the calibration of
209 Seydoux-Guillaume et al. (2002) considers the effect of Th, it is derived for a relatively high
210 temperature range (800–1100 °C). We prefer to use the calibrations of Heinrich et al. (1997)
211 and Pyle et al. (2001) as they rely on natural samples for a lower temperature range (400–700
212 °C). These two calibrations differ, probably because they are based on samples from different
213 metamorphic gradients, and we use both to obtain the range of likely temperature conditions
214 associated with the growth of Mnz–Xtm pairs in direct contact.

215 Electron microprobe element mapping of thin sections (~ 2 x 3 cm areas) was
216 performed at 15 kV, 60 nA, 10 µm beam diameter, 15 µm step size and 4 ms dwell time for
217 the CaK α , AlK α , PK α , FeK α , NaK α lines and the BSE signal. An in-house Matlab© routine
218 was used to identify the different minerals based on image analysis of the combined maps,
219 and to calculate modal abundances (Table 1). The granite mesonorm (Table 1) was calculated
220 following the procedure of Mielke and Winkler (1979) implemented in GCDkit (Janoušek et
221 al. 2006) using whole-rock analyses of Skrzypek et al. (2016) and with all Fe expressed as
222 FeO so as to exclude normative magnetite, since both granites belong to the ilmenite series of
223 Ishihara (1977).

224 Monazite dating by LA-ICP-MS was performed at Gakushuin University, Tokyo, on
225 separated grains mounted in epoxy, using a NWR-213 Nd:YAG laser with a 10 µm spot
226 diameter. The ablated material was carried to an Agilent 8800 single-collector tandem
227 quadrupole ICP-MS for monitoring 204 (Pb+Hg), 206 Pb, 207 Pb, 208 Pb, 232 Th 16 O and 238 U 16 O.
228 Fifteen analyses of unknowns were bracketed by five measurements of 44069 monazite
229 (Aleinikoff et al. 2006) and three of NIST SRM 610 glass (Pearce et al. 1997) for
230 normalization. Namaqualand monazite (1034.4 ± 5.8 Ma concordia age by LA-sector field-

231 ICP-MS; [Gonçalves et al. 2016](#)) was used as a consistency standard and concordant data
232 yielded the following weighted average ages (n=3 concordant analyses out of 5 sequences):
233 $^{206}\text{Pb}/^{238}\text{U}$ age=1061 ± 39 Ma (MSWD=1.40), $^{207}\text{Pb}/^{235}\text{U}$ age=1072 ± 47 Ma (MSWD=3.20),
234 $^{206}\text{Pb}/^{207}\text{Pb}$ age=1092 ± 91 (MSWD=5.20). Error calculations used the standard error (SE, 2σ
235 level) in order to take into account the large number of primary reference material analyses.
236 Considering the typical uncertainty on Pb/U ratios, monazite analyses with a concordance
237 ratio $[\text{U}-\text{U cc}(\%)=(^{206}\text{Pb}/^{238}\text{U date})/(^{207}\text{Pb}/^{235}\text{U date})*100]$ between 97 and 103% are referred
238 to as concordant. The results and full analytical procedure are available as Supplemental
239 Material. Data were plotted with Isoplot 3.76 (Ludwig 2004).

240 **SAMPLE DESCRIPTION**

241 **Samples SHK & SHK2**

242 The main Shimokuhara granite sample (SHK) was collected at the eastern margin of the
243 pluton, a few meters away from the contact with schistose rocks from the Bt zone (Fig. 1).
244 There, the Shimokuhara pluton exhibits a leucocratic, biotite-bearing facies with some K-
245 feldspar phenocrysts (~2 cm in length), plagioclase and quartz aggregates with a noticeable
246 rounded shape (Fig. 2a). Centimeter-scale xenoliths of the neighboring metasediments and
247 small garnet (< 1 mm in diameter) are also observed in the granite. Sample SHK is massive
248 and contains Qtz, Kfs, Pl, Bt with accessory Grt, Ap, Zrn, Mnz, Xtm and secondary Ms, Chl,
249 Ep, Aln, Ttn.

250 In thin section, large (up to 1 cm in diameter) and rounded aggregates of quartz with
251 undulatory extinction dominate (Fig. 2a). K-feldspar phenocrysts ($\text{Or}_{87-93}\text{Ab}_{7-13}$) contain
252 albite rods and locally show the microcline twin. The core of euhedral and concentrically
253 zoned plagioclase ($\text{An}_{18-47}\text{Ab}_{52-81}\text{Or}_1$) is replaced by fine-grained brownish material, probably
254 damourite (Fig. 2a, c). Biotite flakes ($X_{\text{Fe}}=0.68-0.71$; $F=0.27-0.68$ wt%) are interstitial and

255 variably replaced by chlorite (brunsvigite, $X_{Fe}=0.67-0.70$), K-feldspar, muscovite
256 ($F=0.27-0.40$ wt%) and titanite (Fig. 2c). Garnet (up to 400 μm in diameter) is included in K-
257 feldspar phenocrysts and has virtually no inclusion. No mineral preferred orientation is visible
258 under the optical microscope (Fig. 2a).

259 Sample SHK2 was collected 300 m from the mapped contact with metasedimentary
260 rocks. It is a massive granite with Qtz, Kfs, Pl, Bt and accessory Chl, Ilm, Rt, Mnz, Xtm, Zrn,
261 Aln, Ap. Biotite chloritization appears to be less pervasive than in sample SHK.

262 **Samples NAM & NAM2**

263 The main Namera granite sample (NAM) was collected less than a hundred meters away from
264 the contact with migmatitic gneissose rocks from the Kfs–Crd zone (Fig. 1). There, the
265 Namera pluton shows a leucocratic, fine- to coarse-grained biotite-bearing facies and locally
266 contains muscovite, garnet, greenish pinitized cordierite and sillimanite. Several outcrops in
267 the eastern part of the pluton show a weak to moderate gneissosity defined by biotite
268 alignment, but an undeformed facies resembling the Shimokuhara granite is also observed
269 (Fig. 1). The granite is locally cut by cm-thick quartz veins, garnet-bearing aplitic veins and
270 Qtz–Kfs–Ms pegmatites, the latter being nearly parallel to the gneissosity. The outcrop of
271 sample NAM shows cm-thick, garnet-bearing leucocratic veins mostly parallel and locally
272 oblique to the gneissosity. A NE–SW striking fault is mapped in the vicinity of the sampling
273 locality, but no signs of it are visible on the outcrop. Sample NAM has a moderate gneissosity
274 (Fig. 2b) and contains Qtz, Kfs, Pl, Bt with accessory (pinitized) Crd, Grt, Ap, Zrn, Mnz, Xtm
275 and secondary Ms, Chl, Hem.

276 K-feldspar phenocrysts ($\text{Or}_{80-90}\text{Ab}_{10-20}$) exhibit a straight to wavy outline, are locally
277 perthitic and contain albite stringlets. Plagioclase ($\text{An}_{05-39}\text{Ab}_{60-94}\text{Or}_{01-02}$) is found as large
278 crystals (up to 0.5 cm in length), small polygonal grains (~ 100 μm in diameter) or in fine-
279 grained intergrowths with secondary muscovite. Plagioclase locally shows an irregular outline

280 and its core is replaced by skeletal muscovite and minor biotite (Fig. 2b). Quartz shows
281 undulatory extinction and forms slightly elongated ribbons parallel to the gneissose fabric
282 (Fig. 2b). Biotite ($X_{Fe}=0.59-0.63$; $F=0.34-0.56$ wt%) appears as equant flakes or elongate
283 laths that define the gneissosity, and is slightly replaced by chlorite (brunsvigite, $X_{Fe}=0.63$)
284 (Fig. 2b). Garnet (up to 200 μm in diameter) is included in plagioclase. Pools of fine-grained
285 plagioclase and Ms–Bt intergrowths surround minute relicts of pinitized cordierite (200 μm in
286 length). The textural position of both garnet and former cordierite suggests they are of
287 magmatic origin. Secondary muscovite ($F=0.17-0.29$ wt%) is preferentially developed inside
288 K-feldspar where it forms a network of Ms–Qtz veins (Fig. 2d). A few myrmekites are
289 observed at Kfs–Pl contacts.

290 Sample NAM2 is a gneissose granite from an outcrop where no leucocratic veins or
291 pegmatites are observed. It contains Qtz, Kfs, Pl, Bt and accessory Grt, pinitized Crd, Ms,
292 Chl, Mnz, Xtm, Zrn, Ap. The gneissose fabric is slightly stronger than in sample NAM.

293 **Comparison of mineral modes**

294 The whole-rock data published by Skrzypek et al. (2016) show that, despite a different
295 appearance, samples SHK and NAM have a similar major and trace element composition. For
296 further comparison, mineral modal abundances were calculated using whole-rock analyses
297 and EMP mapping of thin sections (Table 1). Granite mesonorm calculations indicate a
298 similar amount of Kfs, Qtz, Pl and Bt in SHK and NAM (Table 1). Element mapping of ~ 3.5
299 x 2 cm thin sections fails to accurately determine the modal amount of phenocrystic phases
300 (Kfs, Qtz, Pl), but can be used for the smaller phyllosilicates. It reveals that the modal amount
301 of Bt in NAM is almost equal to that of Bt plus Chl in SHK (Table 1). Since textural
302 observations indicate that chlorite forms at the expense of biotite, it can be deduced that the
303 original amount of biotite in both samples was identical, as suggested by the mesonorm
304 calculations.

305 **PETROLOGY OF MONAZITE AND ASSOCIATED PHASES**

306 **Sample SHK**

307 Monazite forms euhedral to skeletal grains (~50 to 250 μm in length) with generally few
308 inclusions (Fig. 3a). It is located inside biotite or more commonly at the boundary between
309 biotite and quartz/plagioclase. Monazite grains that were separated from the hand specimen
310 are mostly euhedral, and monazite observed in thin section tends to be more subhedral to
311 anhedral. Large euhedral monazite has micro-cracks along which allanite, hematite and
312 xenotime are observed (Fig. 3b, f), and is surrounded by apatite and a fringe of zoned allanite
313 that becomes REE-poorer towards the rim (Fig. 3b, c). Skeletal monazite is surrounded by
314 large allanite (~100 μm), small Th-U phases (< 30 μm in diameter) and minor xenotime (Fig.
315 3c). Elongate grains of oscillatory-zoned allanite are found at chlorite rims and are locally
316 separated from chlorite by a titanite film (Fig. 3d). In general, monazite occurs together with
317 allanite in the vicinity of chloritized biotite. Xenotime has two modes of occurrence; lone
318 matrix grains form euhedral overgrowths around zircon, whereas tiny anhedral xenotime (<
319 30 μm in length) occurs next to or in contact with altered monazite (Fig. 3b, c, f).

320 Primary and secondary monazite domains are distinguished in both *in situ* and
321 separated grains. Primary domains have sector- or oscillatory-zoned textures that occupy the
322 majority of most monazite grains (Fig. 3e). The primary domains may be subdivided into (1)
323 core domains with a juxtaposition of BSE-bright and BSE-dark sectors, and (2) thin (< 20 μm
324 in width) and BSE-dark outermost rim domains (Fig. 3e). The primary core and outermost rim
325 domains are differentiated by a sharp contrast on BSE images (Fig. 3e). Secondary domains
326 correspond to altered parts of the primary monazite zoning. They are generally associated
327 with the presence of cracks that cross-cut the primary zoning; on BSE images they appear as
328 darker zones up to ~20 μm in width, or as brighter and thin (< 5 μm) veinlets (Fig. 3f).

329 Monazite-(Ce) compositions are dominated by a huttonite-type substitution [$\text{REE}^{3+} +$
330 $\text{P}^{5+} \leftrightarrow (\text{Th,U})^{4+} + \text{Si}^{4+}$] (Fig. 4a). The analyses define a trend with an evolution towards the
331 monazite end-member from the primary core ($X_{\text{hut}}=0.02\text{--}0.13$; $X_{\text{cher}}=0.05\text{--}0.10$;
332 $X_{\text{mnz}}=0.78\text{--}0.92$; 48 analyses on 36 grains) to the outermost rim ($X_{\text{hut}}=0.01\text{--}0.03$;
333 $X_{\text{cher}}=0.05\text{--}0.07$; $X_{\text{mnz}}=0.91\text{--}0.93$; 9 analyses on 9 grains) domains (Fig. 4a, Table 2). This
334 evolution is due to Si + U + Th decrease and P + Light REE (LREE) increase while Y and
335 HREE remain constant. Analyses of the secondary domains follow the huttonitic trend
336 defined by primary domain analyses, with some excess in U \pm Th \pm Pb being responsible for a
337 slight deviation (Fig. 4a). Secondary domain analyses define two subgroups based on Y and U
338 contents; one shows markedly low Y ($\text{Y}_2\text{O}_3=0.55\text{--}1.03$ wt%) and U ($\text{UO}_2 < 0.15$ wt%),
339 whereas the other has Y ($\text{Y}_2\text{O}_3=1.65\text{--}3.27$ wt%) and U ($\text{UO}_2=0.32\text{--}1.22$ wt%) contents in the
340 range of primary domain analyses (Fig. 4b). With respect to primary domains, the Y-poor
341 subgroup of secondary domains is depleted in Y, U, Th, Ca and enriched in both LREE and
342 HREE.

343 Allanite analyses yield low oxide sums (94–97 wt%) that are ascribed to
344 metamictization, since Th-richer spots tend to have lower totals. The composition is mainly
345 that of allanite-(Ce) with recalculated $\text{Fe}^{3+}/\text{Fe}_{\text{tot}}$ ratios of 0.04–0.32 (normalization to 25
346 negative charges) pointing to some ferallanite component, and Al_{tot} (1.99–2.27 a.p.f.u.)
347 indicating some proportion of the Ep-Czo component. The analyses of BSE-bright cores show
348 Σ_{REE} between 0.71 and 0.80 a.p.f.u., negligible actinide contents (< 0.02 a.p.f.u.) and about
349 0.08–0.14 wt% fluorine. One spot from a darker rim overgrowth has a Σ_{REE} of 0.54 a.p.f.u.,
350 actinide abundances below detection limits and about 0.05 wt% fluorine.

351 Lone matrix xenotime (observed in thin section) is enriched in U and Er, Tm, Yb (i.e.
352 HREE with an ionic radius close to that of U), whereas tiny xenotime occurring in monazite
353 alteration textures (separated monazite grains) is enriched in Gd, Tb, Dy (i.e. HREE with an

354 ionic radius close to that of Th) and slightly in Ce and Th. When in direct contact with
355 monazite, xenotime is always adjacent to the BSE-dark, Y-poor secondary domains (Fig. 3f).
356 Six analyses of Y-poor secondary monazite domains in contact with xenotime show a nearly
357 constant $X_{(HREE,Y)}$ (0.060 ± 0.006) and yield temperature estimates of 471 and 562 °C with the
358 calibration of Pyle et al. (2001) and Heinrich et al. (1997), respectively.

359 The tiny Th–U phases (< 30 µm in diameter) are not easily quantified but valid
360 analyses (not influenced by the surrounding minerals) yield a constant oxide sum of about 90
361 wt% (Table 2). They correspond to Th-rich ($\text{ThO}_2=51.67\text{--}62.77$ wt%) silicates with
362 significant amounts of U ($\text{UO}_2=2.14\text{--}12.82$ wt%), P ($\text{P}_2\text{O}_5=0.71\text{--}9.21$ wt%) and Y
363 ($\text{Y}_2\text{O}_3=0.84\text{--}3.40$ wt%). Their formula approaches (Th, U, REE)(Si, P)O₄ with the missing 10
364 wt% being ascribed to free H₂O (Table 2); they can be considered as a monoclinic (huttonite;
365 note that monazite is also monoclinic) or tetragonal (thorite) polymorph of (hydrous) ThSiO₄
366 (Fig. 4c). Electron microprobe age dating of the Th–U phases was attempted due to their high
367 actinide content. The cores of euhedral grains (~30 µm in diameter) included in a K-feldspar
368 phenocryst yield Th–U–Pb dates of 369 ± 6 and 262 ± 7 Ma, whereas the rims show much
369 younger dates of $23\text{--}21 \pm 3$ Ma. These inclusions are, however, not related to monazite and
370 their ages are not discussed further. The other, generally smaller (< 20 µm) Th–U phases
371 occur in the matrix and are always associated with allanite around anhedral monazite; one
372 grain preserves a Th–U–Pb date of 58 ± 5 , three grains yield $15\text{--}14 \pm 2\text{--}3$ Ma and four other
373 grains have PbO below the detection limit.

374 **Sample SHK2**

375 Large (100 µm in diameter) and euhedral monazite grains surrounded by a thin fringe of
376 Aln–Ap with local xenotime and Th–U phases are common, but skeletal aggregates
377 associated with more abundant apatite are also observed (see Supplemental Material for BSE
378 images). Monazite mostly preserves a sector zoning pattern that is affected by micro-cracks

379 and locally riddled with tiny holes. One euhedral and zoned allanite (~ 500 μm in length) is
380 entirely included in a plagioclase grain within a Kfs phenocryst and is regarded as primary in
381 origin. Other allanite occurrences correspond to thin (~ 50 μm in diameter) laths next to
382 monazite or along the cleavages of chloritized biotite. Large matrix xenotime (~ 100 μm in
383 diameter) shows oscillatory zoning cross-cut by BSE-dark zones. Overall, the textures are
384 similar to those observed in SHK, with more occurrences of large euhedral monazite that
385 might be correlated with the lesser degree of chloritization.

386 Monazite domains similar to those distinguished in SHK are identified (Fig. 4a, b).
387 The primary domains show a dominant huttonitic substitution and an increase in the monazite
388 component from the core ($X_{\text{hut}}=0.04\text{--}0.15$; $X_{\text{cher}}=0.03\text{--}0.05$; $X_{\text{mnz}}=0.80\text{--}0.92$) to the outermost
389 rim ($X_{\text{hut}}=0.04\text{--}0.07$; $X_{\text{cher}}=0.03\text{--}0.04$; $X_{\text{mnz}}=0.89\text{--}0.94$). A few BSE-dark secondary domains
390 could be analyzed and their composition mostly falls in a subgroup with markedly low Y
391 ($\text{Y}_2\text{O}_3 < 0.77$ wt%) and U ($\text{UO}_2 < 0.05$ wt%) contents. Only one valid analysis of a Th-U
392 phase could be obtained. Like in SHK, it is a Th-rich silicate (Fig. 4c) with a somewhat higher
393 amount of REE ($\Sigma\text{REE}_2\text{O}_3=15.30$ wt%) and PbO below the detection limit.

394 **Sample NAM**

395 Monazite occurs as subhedral, rounded or anhedral grains (~20 to 250 μm in length) with a
396 variable amount of inclusions (Fig. 5a). Monazite is found inside biotite, plagioclase and at
397 the boundary between major minerals. Tiny zircon in contact with monazite is common, and
398 only one relatively large (~100 μm in diameter) and oscillatory-zoned xenotime is found in
399 textural equilibrium with monazite in the matrix. Other xenotime occurrences are scarce,
400 minute inclusions in monazite. Micro-cracks are rare and are not associated with extensive
401 alteration of the original zoning (Fig. 5c, f).

402 Two contrasting domains are observed in both *in situ* and separated monazite. All
403 grains exhibit a primary sector- or oscillatory-zoned part that is randomly cross-cut and

404 replaced by a secondary BSE-dark and inclusion-rich domain (Fig. 5c, e, f). The proportion of
405 primary to secondary domains varies; only a few grains fully preserve their primary zoning
406 (Fig. 5d), most grains exhibit a juxtaposition of both domains, and some grains are dominated
407 by secondary domains in which only patches of primary domains remain (Fig. 5c, e, f). In
408 general, the secondary domains are preferentially developed in monazite core (Fig. 5e) but
409 examples of replacement occurring at the rim are also found (Fig. 5f).

410 Primary domains are nearly inclusion-free, whereas secondary domains are riddled
411 with inclusions that range from a few microns up to $\sim 50 \mu\text{m}$ in diameter (Fig. 5a, e, f). The
412 inclusions occur as single grains or more commonly form multi-phase aggregates with a
413 rounded or tubular shape (Fig. 5g, h). A survey of 906 inclusions in 84 grains reveals the
414 presence of, in order of decreasing abundance: Zrn, Ms, Kfs, Qtz, Hem, Bt, Po, Pl and scarce
415 Chl, Ap, Xtm and Ant (Fig. 6; Supplemental Material). Among these inclusions, Zrn, Ms, Kfs,
416 Qtz, Bt, Po, Pl, Ap and Xtm are thought to have formed during the magmatic or metamorphic
417 stage while Hem, Chl and Ant are considered as later alteration products. The most common
418 assemblages are Ms–Qtz and Qtz–Kfs–Pl±Bt. A significant number of Si-rich inclusions is
419 also observed (Fig. 5g, h); they appear as orange to brownish blebs under the optical
420 microscope, and their EDS spectrum shows a prominent Si peak with additional Al, K, Na, Ca
421 or Fe peaks (Fig. 6a). They are easily damaged during Raman analysis and their spectrum
422 does not reveal any discernible vibration band outside that of the monazite host (Fig. 6b).

423 Primary and secondary domains are clearly distinguished based on their compositions
424 (Fig. 4, Table 2). Analyses from primary domains follow a dominant huttonitic substitution
425 ($X_{hut}=0.01\text{--}0.07$; $X_{cher}=0.06\text{--}0.14$; $X_{mnz}=0.80\text{--}0.94$; 41 analyses on 29 grains), whereas those
426 from secondary domains cluster on a narrow cheralite–monazite exchange trend ($X_{hut}=0\text{--}0.02$;
427 $X_{cher}=0.10\text{--}0.15$; $X_{mnz}=0.84\text{--}0.89$; 29 analyses on 23 grains; Fig. 4a). With respect to primary
428 domains, secondary domains are depleted in Si, LREE and enriched in Ca, Y, U, P, HREE

429 while Th remains constant. The strongest contrast is seen in the Y and U contents (Fig. 4b);
430 they are on average low in primary domains ($Y_2O_3=0.91$ wt%; $UO_2=0.19$ wt%) and
431 significantly higher in secondary ones ($Y_2O_3=2.30$ wt%; $UO_2=1.43$ wt%).

432 Compared to the large matrix xenotime grain, minute xenotime included in monazite
433 is enriched in La, Ce and depleted in U, Er, Tm, Yb. Xenotime inclusions in monazite, like
434 other minerals, always occur inside the secondary domains. Five analyses of secondary
435 monazite domains in contact with included xenotime show a slightly varying $X_{(HREE,Y)}$ (0.089
436 ± 0.018) and yield temperature estimates of 584 and 664 °C with the calibration of Pyle et al.
437 (2001) and Heinrich et al. (1997), respectively.

438 **Sample NAM2**

439 Monazite is found inside Bt, Kfs or between major minerals; it mostly has a euhedral and
440 slightly rounded shape, but skeletal grains are locally present (see Supplemental Material for
441 BSE images). Monazite shows oscillatory or sector zoning cross-cut by BSE-dark zones with
442 tiny holes or inclusions. Only a few inclusions in monazite could be identified in this thin
443 section; these are Zrn, Po, Ms, Xtm, Chl, Hem, Bt, Qtz and K–Al-bearing Si-rich phases. Tiny
444 (< 30 μm in length) grains of skeletal allanite are locally found in between the major minerals
445 or along biotite cleavages. Euhedral to anhedral matrix xenotime is common and shows sector
446 or oscillatory zoning cross-cut by BSE-dark zones next to chloritized biotite. Monazite
447 textures are globally similar to those observed in sample NAM, but one difference is the
448 limited occurrence of tiny allanite in NAM2.

449 Monazite analyses reveal the same contrast between primary and secondary domains
450 as observed in NAM (Fig. 4a, b). Primary domain analyses follow a huttonitic exchange
451 ($X_{hut}=0.02-0.08$; $X_{cher}=0.02-0.06$; $X_{mnz}=0.86-0.97$) and have relatively low Y and U contents
452 ($Y_2O_3=0.42-1.90$ wt%; $UO_2=0.04-0.38$ wt%). Conversely, secondary domain analyses

453 indicate a cheralitic exchange ($X_{hut}=0-0.04$; $X_{cher}=0.01-0.11$; $X_{mnz}=0.85-0.99$) and are
454 commonly enriched in Y and U ($Y_2O_3=1.49-3.03$ wt%; $UO_2=0.15-3.26$ wt%).

455 **MONAZITE GEOCHRONOLOGY**

456 **Sample SHK**

457 Twenty-six analyses were performed on fifteen grains, with two spots (16.4/16.6) located on
458 cracks being rejected due to severe discordance. The remaining 24 analyses are located on
459 primary core (15 spots, $U/Th \leq 0.03$) and outermost rim (9 spots, $U/Th > 0.03$) domains, and
460 13 are concordant. Concordant core analyses show $^{206}Pb/^{238}U$ dates spreading from 116 ± 3 to
461 98 ± 3 Ma (106 Ma on average; Fig. 7a, b) with no clear maximum in the probability density
462 distribution. The three concordant spots from the outermost rim parts yield a weighted
463 average $^{206}Pb/^{238}U$ date of 102 ± 2 Ma (MSWD=1.13, n=3), which is similar to the lower
464 intercept date tentatively calculated with all outermost rim analyses in an inverse Concordia
465 diagram (102 ± 2 Ma, MSWD=2.2, n=9).

466 **Sample NAM**

467 Twenty-six analyses were performed on nineteen grains, with two severely discordant spots
468 (19.8/19.13) being discarded as they are affected by the presence of an inclusion or located at
469 a grain edge. The remaining 24 analyses are clearly differentiated based on their U/Th ratio;
470 they belong to primary (11 spots, $U/Th \leq 0.01$) and secondary (11 spots, $U/Th \geq 0.10$) domains,
471 two spots (20.14/20.15) with an intermediate U/Th ratio (0.02–0.03) being considered as
472 analyses of mixed domains. Primary domain analyses show a significant degree of
473 discordance and their $^{206}Pb/^{238}U$ dates spread between 116 ± 6 and 101 ± 6 Ma, with only one
474 concordant spot (19.15) at 106 ± 5 Ma (Fig. 7d). The latter result agrees with the weighted
475 average $^{206}Pb/^{238}U$ date of 109 ± 2 (MSWD=2.00, n=11) calculated with all primary domain
476 analyses. Secondary domain analyses have a better concordance; 10 spots out of 11 are

477 concordant and their $^{206}\text{Pb}/^{238}\text{U}$ dates spread from 102 ± 3 to 91 ± 2 Ma (Fig. 7d). No clear
478 maximum arises from this spread, and no correlation between $^{206}\text{Pb}/^{238}\text{U}$ date and U/Th ratio
479 is apparent. For example, the two spots with the highest U/Th ratios yield the oldest (19.3:
480 102 ± 2 Ma, U/Th=0.21) and youngest (19.11: 91 ± 2 Ma, U/Th=0.21) $^{206}\text{Pb}/^{238}\text{U}$ dates of the
481 distribution (Fig. 7c).

482 **MONAZITE ALTERATION PROCESSES**

483 The SHK and NAM granite samples have, despite contrasting textures (Fig. 2a, b), nearly
484 similar mineral modes (Table 1), whole-rock compositions, U–Pb zircon ages (Skrzypek et al.
485 2016) and U–Pb monazite ages for primary domains (Fig. 7b, d). These similarities are used
486 to demonstrate that the different monazite alteration textures are not due to initial
487 compositional differences, but to the respective P – T and chemical conditions of the
488 metamorphic overprintings that affected the granites.

489 **Monazite replacement at low to medium temperature (Shimokuhara granite)**

490 Monazite in SHK and SHK2 mostly consists of primary domains for which sector or
491 oscillatory zoning and compositional variations along a single exchange trend suggest a
492 magmatic origin (Figs. 3e and 4a). However, numerous observations indicate alteration of
493 primary monazite. The change from a euhedral to a skeletal shape points to a variable degree
494 of monazite dissolution. Allanite, apatite, xenotime and Th–U phases – i.e. secondary
495 products that partly use elements originally contained in monazite – develop directly adjacent
496 to altered monazite, along its margins or cracks (Fig. 3b, c, f). Euhedral allanite is also found
497 farther from monazite along chlorite cleavages (Fig. 3d), indicating some REE mobility since
498 monazite is the main, primary LREE-carrier in the rock. Monazite replacement by Aln–Ap is
499 dominant, but recrystallization is additionally observed in the secondary, porous domains that
500 developed in cracks or at the rim of some grains (Fig. 3b, f).

501 The formation of hydrous phases such as allanite and chlorite next to altered monazite,
502 and indications of (limited) element transport strongly suggest that monazite replacement
503 involved the action of an aqueous fluid. The secondary domains also bear similarities with the
504 textures reported for monazite alteration experiments in the presence of fluids (e.g.
505 Hetherington et al. 2010). In several of these experiments the composition of secondary
506 monazite shows LREE enrichment and Y, Ca, Th, U depletion (Harlov et al. 2011; Williams
507 et al. 2011; Grand'homme et al. 2018), as observed for the Y-poor subgroup of secondary
508 domains (Fig. 4b). The effects of aqueous fluid on monazite dissolution were investigated for
509 a wide range of P – T conditions and fluid compositions (e.g. Oelkers and Poitrasson 2002;
510 Schmidt et al. 2007; Hetherington et al. 2010; Budzyń et al. 2011; 2015; 2017; Harlov et al.
511 2011; Williams et al. 2011; Grand'homme et al. 2018; Trail 2018). The main outcome of
512 experimental studies is that alkali-bearing fluids (NaOH, KOH) more efficiently lead to
513 dissolution and recrystallization, while observations of natural samples insist on the role of
514 halogens in enhancing monazite dissolution (e.g. Förster 2001; Didier et al. 2013).

515 In addition to H₂O, a source of Ca (\pm Al, Si) has to be identified to explain the growth
516 of Aln–Ap after monazite (Fig. 3b, c). In a similar case of magmatic monazite replacement in
517 S-type granitoids, Broska et al. (2005) proposed plagioclase (for Ca) and biotite (for Al, Si, F)
518 as likely sources. In sample SHK biotite and the Ca-rich core of large plagioclase are
519 extensively altered (Fig. 2a, c), and biotite chloritization could have released some F
520 (~0.27–0.68 wt%) that was subsequently incorporated in allanite (~0.08–0.14 wt%). To
521 explain monazite replacement by Aln–Ap in granitoids, Broska and Siman (1998) proposed a
522 reaction that involves anorthite breakdown but not biotite chloritization. Following the
523 minerals observed in monazite alteration textures, we use the mineral compositions measured
524 in SHK to present a stoichiometrically-balanced reaction that tries to conserve most elements
525 (except HREE–Y, Th–U and F; see Supplemental material for the calculation procedure). The

526 main uncertainty in our approach lies in the elements that potentially arrived and escaped with
527 the fluid (+Ca, Si; -F, Na, K). The proposed reaction is: $1 \text{ Mnz} + 5.462 \text{ Pl} + 4.041 \text{ Bt} + 3.828$
528 $\text{Qtz} + 3.078 \text{ H}_2\text{O} + 1.148 \text{ Ca}^{2+} \rightarrow 1.095 \text{ Aln} + 0.316 \text{ Ap} + 1.317 \text{ Chl} + 1 \text{ Ttn} + 3.268 \text{ Kfs} + 1$
529 $\text{Ms} + 2.780 \text{ Ab} (+ 0.013 \text{ HREE-Y} + 0.089 \text{ Th-U} + 0.300 \text{ F})$. The slight excess of HREE-Y
530 and Th-U can be accounted for by the occurrence of tiny xenotime and Th-U phases in the
531 monazite alteration textures (Fig. 3b, c, f), while the high proportions of Kfs and Ab
532 compared to those observed in the chloritization textures suggest that some K and Na are
533 instead stored in damourite or were lost in the fluid together with excess F. The major
534 alteration process can therefore be explained by a nearly balanced replacement reaction that
535 leaves magmatic monazite as a metastable relict.

536 The formation of the observed replacement textures requires an increase in Ca activity
537 and H₂O influx. At the magmatic stage, the first condition can be met and lead to monazite
538 replacement by Aln-Ap (Dini et al. 2004), but contemporaneous chlorite growth is unlikely.
539 Conversely, both conditions are satisfied by hydrothermal alteration for which plagioclase
540 resorption and biotite chloritization are commonly reported (e.g. Alderton et al. 1980;
541 Yuguchi et al. 2015). The results of Mnz-Xtm thermometry suggest that the rare secondary
542 domains in SHK formed at 471–562 °C. This range agrees with temperature estimates for the
543 regional overprint in the neighboring schist zone (450–550 °C; Ikeda 2004), but the upper
544 temperature limit conflicts with the widespread occurrence of chlorite. This could suggest that
545 limited monazite recrystallization actually occurred at lower-amphibolite facies conditions (>
546 500 °C), whereas later monazite replacement was due to a more pervasive hydrothermal
547 alteration of the granite at greenschist facies conditions (< 500 °C). Similar monazite
548 replacement textures were reported in rocks that experienced peak metamorphic temperatures
549 of 340 °C (Poitrasson et al. 2000), 550–600 °C (Finger et al. 1998) and up to 685–825 °C
550 (Broska et al. 2005). Although the *P-T* conditions at which monazite replacement occurs are

551 likely controlled by the whole-rock Ca and Al contents (e.g. Spear, 2010), we propose that the
552 textures can hint at a low- or high-grade origin. The presence of chlorite, fractured monazite
553 and allanite growing farther from monazite would indicate the dominance of pervasive fluid
554 circulation at greenschist facies conditions, whereas the formation of Aln–Ap coronas should
555 reflect the increasing role of diffusion at higher metamorphic grade (Broska et al. 2005;
556 Finger et al. 1998; 2016; Ondrejka et al. 2012).

557 **Monazite recrystallization at high temperature (Namera granite)**

558 Monazite is the dominant LREE-rich phase observed in samples NAM and NAM2. It is
559 composed of sector- and oscillatory-zoned primary domains whose composition lies on the
560 same huttonitic trend as that defined by primary domain analyses from sample SHK (Figs. 4a
561 and 5d). This supports the magmatic origin of monazite in both samples. A significant part of
562 monazite is also occupied by secondary domains enriched in Ca, Y, U and P (Fig. 4). The
563 formation of secondary domains generally preserves the shape of the original magmatic grain,
564 and it is necessary to clarify whether this pseudomorphic recrystallization occurred at the
565 solid state or under the action of a fluid phase.

566 Primary and secondary domains are separated by a sharp boundary on BSE images,
567 and their composition is clearly distinct (Figs. 4 and 5c, e, f). This stands against
568 intracrystalline diffusion, which should result in more gradual changes in terms of texture (see
569 the diffusion zone imaged by Gardés et al. 2006) and composition (e.g. Cherniak et al. 2004).
570 In addition, BSE images show that recrystallization does not necessarily start from the rim
571 and proceed inwards, but that a preferential recrystallization of the monazite core is dominant
572 (Figs. 5e and 7c). The latter observation suggests that a mobile medium was able to make its
573 way up to the more unstable core, possibly through precursor cracks. Thus, the action of a
574 fluid phase is inferred to explain the selective dissolution of primary monazite. Dissolution
575 was selective; it is striking that the primary domains have a narrow compositional range,

576 although a larger spread might be expected by analogy with the composition of primary
577 monazite in sample SHK, which has the same bulk composition as sample NAM (Fig. 4a).
578 The primary domains that are presently observed must have been the most robust parts during
579 dissolution, whereas we suppose that the originally Th–U-richer monazite core was more
580 reactive, more porous to allow fluid circulation, hence preferentially dissolved. The different
581 solubilities of the initial domains could have been due to a higher degree of disequilibrium
582 with respect to the fluid, and/or to denser radiation damage in the supposedly Th–U-rich core.

583 Dissolution of the primary domains had to be followed by precipitation of secondary
584 monazite at exactly the same place in order to explain the pseudomorph texture (Fig. 5f). Both
585 characteristics are accounted for by the dissolution-reprecipitation process detailed by Putnis
586 (2002). A key aspect of this process is that a fluid-mineral interface has to be maintained so
587 that recrystallization can proceed (Putnis and Putnis 2007). In samples NAM and NAM2,
588 recrystallization corresponds to the transformation of primary huttonitic monazite into
589 secondary cheralitic monazite (Fig. 4a). According to the unit cell parameters of natural
590 monazite-(Ce) (Ni et al. 1995), huttonite (Taylor and Ewing 1978) and $\text{Ca}_{0.5}\text{Th}_{0.5}\text{PO}_4$ (Terra et
591 al. 2008), this transformation should result in a unit cell volume decrease of at least ~0.14%.
592 Although limited, the volumetric decrease indicates that a porosity could be maintained and
593 progressively filled by inclusions, the latter being distinctively abundant in the secondary
594 domains (Fig. 5a, e, f).

595 The major factor controlling the spatial and temporal extent of the dissolution-
596 reprecipitation process is the fluid composition (Putnis 2009). In the case of NAM and NAM2
597 samples, it was a fluid able to initially dissolve monazite and to reprecipitate not only new
598 monazite but also the whole range of inclusions that are found in the secondary domains (Zrn,
599 Ms, Kfs, Qtz, Bt, Po, Pl, Ap, Xtm). Similar inclusions are also reported in zircon from the
600 same sample (Qtz, Pl, Kfs, Ms, Bt, Hem, Ap, Xtm; Skrzypek et al. 2016). Because of these

601 constraints, the fluid medium is thought to be anatectic melt. Dissolution, transport and
602 reprecipitation of zircon, apatite or xenotime in the presence of alkaline fluids has been
603 reported (e.g. Tomaschek et al. 2003; Rubatto et al. 2008; Harlov 2011; Broom-Fendley et al.
604 2016), but at low pressure the solubility of both monazite and zircon is higher in granitic melt
605 than in aqueous fluid (e.g. Montel 1986; Watson 1979; Ayers and Watson 1991). In addition,
606 the rounded or tubular shape (Fig. 5g, h) and the nature of the most abundant multi-phase
607 inclusions in recrystallized monazite (Si-rich (melt?), Qtz–Kfs–Pl, Qtz–Ms assemblages)
608 strongly suggest that a hydrous granitic melt crystallized in the pores. A similar texture with
609 numerous and tiny multi-phase inclusions is reported for metamorphic monazite that grew in
610 the presence of leucogranitic melt (Bea and Montero, 1999).

611 The origin of the anatectic liquid that is thought to have favored monazite
612 recrystallization is debatable. Although small amounts of partial melt are difficult to
613 recognize, the Ms–Qtz network texture observed in thin section (Fig. 2d) might be evidence
614 of internal or external melt percolation. On the one hand, regional metamorphism in the
615 neighboring Kfs–Crd zone peaked at 2–3 kbar/590–675 °C (Ikeda 2004) and locally reached
616 the range of H₂O-present melting reactions for granitic compositions (e.g. Weinberg and
617 Hasalová 2015). The Namera granite might therefore have experienced a small degree of *in*
618 *situ* wet melting, which produced a liquid that could dissolve monazite, zircon and xenotime.
619 The latter mineral, which is scarcely observed in the matrix and relatively U-rich, represents a
620 likely source for U and Y enrichment in recrystallized monazite. On the other hand,
621 metasedimentary rocks in the Kfs–Crd zone show leucocratic layers that are ascribed to
622 partial melting (Brown 1998; Kawakami and Ikeda, 2003), and this external melt could
623 equally have infiltrated the Namera granite. The presence of undeformed Grt-bearing
624 leucocratic veins and Qtz–Kfs–Ms pegmatite on NAM outcrop supports this view, but a
625 similar observation is unfortunately not made on NAM2 outcrop. Melt provided by the

626 metasedimentary rocks would also have the advantage of being in greater disequilibrium with
627 the granitic assemblage, thereby enhancing monazite dissolution. It is therefore proposed that
628 monazite recrystallization occurred at 584–664 °C and was facilitated by the infiltration of
629 melt possibly derived from the neighboring metasedimentary rocks.

630 **CONSEQUENCES FOR MONAZITE GEOCHRONOLOGY**

631 **Preservation of magmatic age**

632 In monazite from sample SHK, the primary core and outermost rim domains show no
633 difference in $^{206}\text{Pb}/^{238}\text{U}$ date, and concordant rim analyses yield a weighted average $^{206}\text{Pb}/^{238}\text{U}$
634 date of 102 ± 2 Ma (Fig. 7a, b). In sample NAM, the only concordant analysis of primary
635 monazite domain yields 106 ± 5 Ma (Fig. 7d). Both results are within error of the U–Pb
636 zircon ages of 105 ± 3 Ma and 105 ± 2 Ma derived from the same SHK and NAM samples,
637 respectively (Skrzypek et al. 2016). These age similarities, together with well-defined sector
638 and oscillatory zoning patterns, support a magmatic origin for both zircon and monazite, and
639 indicate that the age of magmatic crystallization is preserved in the primary monazite
640 domains. Previous works similarly reported that monazite may partly retain its magmatic age
641 in meta-igneous rocks metamorphosed up to ~ 700 °C, despite subsequent alteration (Finger et
642 al. 1998, 2016; Townsend et al. 2000). This view appears fully valid for sample SHK in which
643 the greenschist facies regional overprint did not lead to total monazite replacement, which
644 allows the magmatic age to be measured with a 10 μm laser spot. The magmatic age is less
645 well preserved in monazite from sample NAM, but is still accessible with the analytical
646 approach used in this study. The main observation is that the primary domain analyses are
647 commonly discordant (Fig. 7d). Given that such a discordance is not observed in SHK, it is
648 suspected that the upper-amphibolite facies metamorphic overprint was responsible for some

649 disturbance of the primary isotopic system in NAM. The BSE images of primary domains,
650 however, do not hint at a perturbation of the original, magmatic sector zoning (Figs 5 and 7c).

651 **Identification of alteration age**

652 Age dating of the secondary monazite domains in SHK was not attempted due to their small
653 size. In trying to analyze similar narrow veinlets by ion probe, Townsend et al. (2000) could
654 obtain nothing but mixed ages. Moreover, two spots located on micro-cracks show that severe
655 discordance is to be expected for the secondary domains (spot 16.6 in Fig. 7a). A few analyses
656 of the Th–U phases found next to altered monazite yield one Th–U–Pb date of 58 ± 5 and
657 three of $15\text{--}14 \pm 2\text{--}3$ Ma, with four nearly Pb-free spots (Fig. 4d). Because the Th–U phases
658 are tiny anhedral grains that are thought to host ~ 10 wt% H₂O, the probability of radiogenic
659 Pb loss is high and the Th–U–Pb dates should be treated with extreme caution. We can simply
660 remark that the oldest Th–U–Pb date (58 ± 5 Ma) agrees with the apatite fission track age of
661 57.4 ± 5 Ma that is reported for a granodiorite sample in the southern part of the Iwakuni-
662 Yanai area and ascribed to final exhumation of the Ryoke belt (Okudaira et al. 2001). It is
663 therefore possible that monazite replacement associated with chloritization actually occurred
664 during the Paleogene, when granitic rocks were ultimately brought closer to the surface.

665 The extensive recrystallization of secondary monazite in NAM gives the opportunity
666 to date the new domains *in situ*. However, the age of recrystallization is difficult to constrain
667 from the spread of concordant $^{206}\text{Pb}/^{238}\text{U}$ dates (102 ± 3 to 91 ± 2 Ma) that is obtained for
668 secondary domains (Fig. 7d). A first interpretation would be to consider all results as true
669 recrystallization ages, in which case a ca. 10 Ma duration could be ascribed to the whole
670 dissolution-reprecipitation process. A second interpretation is to consider that the results
671 reflect isotopic mixing between the primary and youngest secondary compositions. This view
672 is supported by several examples of Pb incorporation and incomplete isotopic resetting during
673 monazite recrystallization by dissolution-reprecipitation (Teufel and Heinrich 1997; Seydoux-

674 Guillaume et al. 2002, 2012; Grand'Homme et al. 2016). In such a case, the youngest
675 $^{206}\text{Pb}/^{238}\text{U}$ date of 91 ± 2 Ma can be considered as the minimum age for monazite
676 recrystallization.

677 **Resolving the zircon-monazite age discrepancy and the age of high-*T* metamorphism**

678 No discrepancy between U–Pb zircon (105 ± 3 Ma; Skrzypek et al. 2016) and monazite dates
679 (102 ± 2 Ma) is revealed for sample SHK, because monazite recrystallization remains limited.
680 The CHIME monazite dates of 87.3 ± 1.6 and 86.6 ± 2.1 Ma reported for the Shimokuhara
681 granite (Suzuki et al. 1996) were obtained from a sample collected at the northern edge of the
682 pluton, next to a fault zone (K. Suzuki, personal communication). The best way to explain
683 these younger CHIME results is to assume that monazite recrystallization was more
684 pronounced in that sample, so that the CHIME dates actually constrain monazite
685 recrystallization during regional metamorphism in the Ms-Crd zone ($\sim 500\text{--}550$ °C; Ikeda,
686 2004). Conversely, dominant monazite replacement in SHK should be associated with lower
687 temperature chloritization (< 500 °C), and the Th–U–Pb dates obtained from Th–U phases
688 next to replaced monazite suggest that this alteration stage might be significantly younger
689 (Paleogene ?) and unrelated to regional metamorphism.

690 For sample NAM, the U–Pb age of secondary monazite domains ($102\text{--}91$ Ma) can be
691 up to ~ 10 Ma younger than that of magmatic monazite (106 ± 5 Ma) and zircon (105 ± 2 Ma;
692 Skrzypek et al. 2016). The comparison between our monazite analyses and those of Suzuki et
693 al. (1996) clearly shows that the CHIME dates ($91\text{--}89.9 \pm 3.2$ Ma; Suzuki et al. 1996) were
694 calculated by grouping spots from primary and secondary domains. Because the secondary
695 domains are U-rich and thus have a lower analytical uncertainty, they presumably had more
696 weight in the calculation of the Th* vs. Pb isochron, which led to results of $91\text{--}90$ Ma (Suzuki
697 et al. 1996). As confirmed by our combined petrological and geochronological data, the age of

698 ca. 91 Ma cannot be ascribed to magmatic crystallization but rather reflects monazite
699 recrystallization during a subsequent metamorphic overprint.

700 The present work proposes that the Kfs–Crd zone was still subjected to suprasolidus
701 conditions at ~ 91 Ma, i.e. about 10 Ma later than in the deeper Grt–Crd zone (U–Pb zircon
702 ages of 103–97 Ma; Nakajima et al. 2013; Skrzypek et al. 2018). It is another argument for
703 the diachronous origin of the metamorphic field gradient exposed in the Ryoike belt (Skrzypek
704 et al. 2016), and agrees with the persistence of medium-*T* conditions until 89 ± 5 Ma, as
705 suggested by U–Pb monazite ages obtained in a gneiss sample from the Kfs–Crd zone
706 (Skrzypek et al. 2018). The accumulation of petrochronological data reveals that in the Ryoike
707 belt – the type locality for low-*P*/high-*T* metamorphism – the age at which high-*T* conditions
708 ended seems to become younger with decreasing depth in the metamorphic section.

709 **CONCLUSIONS AND IMPLICATIONS**

710 We investigated two plutons for which the selected hand specimens appear as fresh, massive
711 or deformed biotite-granites. Under the microscope, the major minerals are not significantly
712 altered, except for plagioclase damouritization and variable biotite chloritization in the
713 massive granite, and the occurrence of Qtz–Ms veinlets and pinitization in the deformed
714 granite. However, the shape and/or composition of magmatic monazite is commonly altered in
715 both granites. The versatility of this accessory mineral offers a unique chance to constrain the
716 nature and timing of post-magmatic metasomatic events that are not easily detected otherwise.

717 *Monazite alteration textures – clues to metasomatic conditions*

718 The two plutons arguably have a similar composition, but differences in their post-magmatic
719 histories led to contrasting monazite alteration processes. Depending on the response of the
720 granitic assemblage to post-emplacement *P–T* and chemical conditions, the interaction
721 between the metamorphosed major and accessory minerals and a fluid medium will result in
722 monazite replacement or recrystallization. On the one hand, the hydration of a granitic

723 assemblage at low temperature (< 500 °C) will trigger the alteration of Ca-plagioclase and the
724 chloritization of biotite. This will enrich the externally-derived aqueous fluid in Ca+Si+Al±F
725 and favor *monazite replacement* by allanite and apatite. We introduce a new reaction that
726 accounts for this process and that is expected in most monazite-bearing granitoids affected by
727 greenschist facies hydrothermalism. On the other hand, a limited amount of hydrous melt,
728 probably of external origin and percolating through the granitic assemblage, can trigger
729 *monazite recrystallization* by dissolution-precipitation at upper-amphibolite facies
730 conditions (> 600 °C). The recrystallized monazite domains are expected to host inclusions,
731 and their new composition will be controlled by the dissolution of other phases in the
732 presence of melt, with for instance Y and U enrichment reflecting xenotime resorption.

733 *Monazite alteration textures – a chance for dating the thermal history*

734 Age dating of monazite alteration textures can yield information on both the magmatic and
735 subsequent alteration stages. Monazite *replacement* leaves primary domains that show no
736 detectable modification of the isotopic system and preserve the age of magmatic
737 crystallization. The minute Th–U-rich alteration products of monazite can additionally yield
738 precise constraints on the timing of low-*T* metasomatism. Partial monazite *recrystallization*
739 causes a disturbance of the isotopic system in primary domains and limits the access to the
740 magmatic crystallization age. It also produces secondary domains that are large enough to be
741 analyzed, but in which an incomplete resetting of the primary isotopic signature complicates
742 the interpretation of the alteration age. The recrystallized domains nevertheless provide a
743 minimum age for the end of high-*T* conditions. Regardless of the process involved, monazite
744 alteration textures offer the possibility to date precise steps of a high- to low-*T*, post-magmatic
745 thermal evolution.

746 **ACKNOWLEDGMENTS**

747 This work benefited from funding by the Japanese Society for the Promotion of Science (JSPS
748 postdoctoral fellowship to E.S., JSPS grant No. 25-03715 to T. Hirajima). We acknowledge
749 financial support by T. Kawakami (Kyoto University “Ishizue” program), and thank T. Hirata
750 and H. Iwano for their help with preliminary analyses in Kyoto, and C. Mattinson for
751 facilitating monazite analyses. E.S. wishes to thank T. Kato (Nagoya University) for sharing
752 his knowledge on microprobe analysis of monazite. We extend our thanks to J.F. Molina and
753 two other referees for useful review comments, and to C.J. Hetherington for insightful
754 editorial handling of the manuscript.

755 **REFERENCES CITED**

- 756 Alderton, D.H.M., Pearce, J.A., and Potts, P.J. (1980) Rare earth element mobility during
757 granite alteration: Evidence from southwest England. *Earth and Planetary Science Letters*,
758 49, 149–165.
- 759 Aleinikoff, J.N., Schenck, W.S., Plank, M.O., Srogi, L., Fanning, C.M., Kamo, S.L., and
760 Bosbyshell, H. (2006) Deciphering igneous and metamorphic events in high-grade rocks
761 of the Wilmington Complex, Delaware: Morphology, cathodoluminescence and
762 backscattered electron zoning, and SHRIMP U-Pb geochronology of zircon and monazite.
763 *Geological Society of America Bulletin*, 118, 39–64.
- 764 Ayers, J.C., and Watson, E.B. (1991) Solubility of apatite, monazite, zircon, and rutile in
765 supercritical aqueous fluids with implications for subduction zone geochemistry.
766 *Philosophical Transactions - Royal Society of London, A*, 335, 365–375.
- 767 Be Mezeme, E.B., Cocherie, A., Faure, M., Legendre, O., and Rossi, P. (2006) Electron
768 microprobe monazite geochronology of magmatic events: examples from Variscan
769 migmatites and granitoids, Massif Central, France. *Lithos*, 87, 276–288.

- 770 Bea, F., and Montero, P. (1999) Behavior of accessory phases and redistribution of Zr, REE,
771 Y, Th, and U during metamorphism and partial melting of metapelites in the lower crust:
772 an example from the Kinzigite Formation of Ivrea-Verbano, NW Italy. *Geochimica et*
773 *Cosmochimica Acta*, 63, 1133–1153.
- 774 Bence, A.E., and Albee, A.L. (1968) Empirical correction factors for the electron
775 microanalysis of silicates and oxides. *The Journal of Geology*, 76, 382–403.
- 776 Broom-Fendley, S., Styles, M.T., Appleton, J.D., Gunn, G., and Wall, F. (2016) Evidence for
777 dissolution-precipitation of apatite and preferential LREE mobility in carbonatite-
778 derived late-stage hydrothermal processes. *American Mineralogist*, 101, 596–611.
- 779 Broska, I., and Siman, P. (1998) The breakdown of monazite in the West-Carpathian Veporic
780 orthogneisses and Tatric granites. *Geologica Carpathica*, 49, 161–167.
- 781 Broska, I., Williams, C.T., Janák, M., and Nagy, G. (2005) Alteration and breakdown of
782 xenotime-(Y) and monazite-(Ce) in granitic rocks of the Western Carpathians, Slovakia.
783 *Lithos*, 82, 71–83.
- 784 Brown, M. (1998) Unpairing metamorphic belts: P-T paths and a tectonic model for the
785 Ryoke Belt, southwest Japan. *Journal of Metamorphic Geology*, 16, 3–22.
- 786 Budzyn, B., Harlov, D.E., Williams, M.L., and Jercinovic, M.J. (2011) Experimental
787 determination of stability relations between monazite, fluorapatite, allanite, and REE-
788 epidote as a function of pressure, temperature, and fluid composition. *American*
789 *Mineralogist*, 96, 1547–1567.
- 790 Catlos, E.J. (2013) Versatile Monazite: resolving geological records and solving challenges in
791 materials science: Generalizations about monazite: Implications for geochronologic
792 studies. *American Mineralogist*, 98, 819–832.
- 793 Cherniak, D.J., Watson, E.B., Grove, M., and Harrison, T.M. (2004) Pb diffusion in monazite:
794 A combined RBS/SIMS study. *Geochimica et Cosmochimica Acta*, 68, 829–840.

- 795 Didier, A., Bosse, V., Boulvais, P., Bouloton, J., Paquette, J.-L., Montel, J.-M., and Devidal,
796 J.-L. (2013) Disturbance versus preservation of U-Th-Pb ages in monazite during fluid-
797 rock interaction: Textural, chemical and isotopic in situ study in microgranites (Velay
798 Dome, France). *Contributions to Mineralogy and Petrology*, 165, 1051–1072.
- 799 Dini, A., Rocchi, S., and Westerman, D.S. (2004) Reaction microtextures of REE–Y–Th–U
800 accessory minerals in the Monte Capanne pluton (Elba Island, Italy): a possible indicator
801 of hybridization processes. *Lithos*, 78, 101–118.
- 802 Engi, M. (2017) Petrochronology based on REE-minerals: monazite, allanite, xenotime,
803 apatite. *Reviews in Mineralogy and Geochemistry*, 83, 365–418.
- 804 Finger, F., Broska, I., Roberts, M.P., and Schermaier, A. (1998) Replacement of primary
805 monazite by apatite-allanite-epidote coronas in an amphibolite facies granite gneiss from
806 the eastern Alps. *American Mineralogist*, 83, 248–258.
- 807 Finger, F., Krenn, E., Schulz, B., Harlov, D., and Schiller, D. (2016) “Satellite monazites” in
808 polymetamorphic basement rocks of the Alps: Their origin and petrological significance.
809 *American Mineralogist*, 101, 1094–1103.
- 810 Förster, H.-J. (2001) Synchronite-(Y)–synchronite-(Ce) solid solutions from Markersbach,
811 Erzgebirge, Germany: REE and Th mobility during high-T alteration of highly
812 fractionated aluminous A-type granites. *Mineralogy and Petrology*, 72, 259–280.
- 813 Foster, G., Parrish, R.R., Horstwood, M.S., Chenery, S., Pyle, J., and Gibson, H.D. (2004)
814 The generation of prograde P–T–t points and paths; a textural, compositional, and
815 chronological study of metamorphic monazite. *Earth and Planetary Science Letters*, 228,
816 125–142.
- 817 Gardés, E., Jaoul, O., Montel, J.-M., Seydoux-Guillaume, A.-M., and Wirth, R. (2006) Pb
818 diffusion in monazite: An experimental study of $Pb^{2+} + Th^{4+} \leftrightarrow 2 Nd^{3+}$ interdiffusion.
819 *Geochimica et Cosmochimica Acta*, 70, 2325–2336.

- 820 Geological Survey of Japan (2012) Seamless digital geological map of Japan 1: 200,000. July
821 3, 2012 version. Research Information Database DB084. Geological Survey of Japan,
822 National Institute of Advanced Industrial Science and Technology (ed.).
- 823 Gonçalves, G.O., Lana, C., Scholz, R., Buick, I.S., Gerdes, A., Kamo, S.L., Corfu, F.,
824 Marinho, M.M., Chaves, A.O., and Valeriano, C. (2016) An assessment of monazite from
825 the Itambé pegmatite district for use as U–Pb isotope reference material for microanalysis
826 and implications for the origin of the “Moacyr” monazite. *Chemical Geology*, 424, 30–50.
- 827 Grand’Homme, A., Janots, E., Seydoux-Guillaume, A.-M., Guillaume, D., Bosse, V., and
828 Magnin, V. (2016) Partial resetting of the U-Th-Pb systems in experimentally altered
829 monazite: Nanoscale evidence of incomplete replacement. *Geology*, 44, 431–434.
- 830 Grand’Homme, A., Janots, E., Seydoux-Guillaume, A.M., Guillaume, D., Magnin, V.,
831 Hövelmann, J., Höschen, C., and Boiron, M.C. (2018) Mass transport and fractionation
832 during monazite alteration by anisotropic replacement. *Chemical Geology*, 484, 51–68.
- 833 Harlov, D.E. (2011) Formation of monazite and xenotime inclusions in fluorapatite
834 megacrysts, Gloserheia Granite Pegmatite, Froland, Bamble Sector, southern Norway.
835 *Mineralogy and Petrology*, 102, 77.
- 836 Harlov, D.E., Wirth, R., and Hetherington, C.J. (2011) Fluid-mediated partial alteration in
837 monazite: The role of coupled dissolution-reprecipitation in element redistribution and
838 mass transfer. *Contributions to Mineralogy and Petrology*, 162, 329–348.
- 839 Harrison, T.M., McKeegan, K.D., and LeFort, P. (1995) Detection of inherited monazite in
840 the Manaslu leucogranite by $^{208}\text{Pb}/^{232}\text{Th}$ ion microprobe dating: crystallization age and
841 tectonic implications. *Earth and Planetary Science Letters*, 133, 271–282.
- 842 Hawkins, D.P., and Bowring, S.A. (1997) U-Pb systematics of monazite and xenotime: case
843 studies from the Paleoproterozoic of the Grand Canyon, Arizona. *Contributions to*
844 *Mineralogy and Petrology*, 127, 87–103.

- 845 Heinrich, W., Andrehs, G., and Franz, G. (1997) Monazite–xenotime miscibility gap
846 thermometry. I. An empirical calibration. *Journal of Metamorphic Geology*, 15, 3–16.
- 847 Herzig, C.T., Kimbrough, D.L., Tainosho, Y., Kagami, H., Iizumi, S., and Hayasaka, Y.
848 (1998) Late Cretaceous U/Pb zircon ages and Precambrian crustal inheritance in Ryoke
849 granitoids, Kinki and Yanai districts, Japan. *Geochemical journal*, 32, 21–31.
- 850 Hetherington, C.J., Harlov, D.E., and Budzyń, B. (2010) Experimental metasomatism of
851 monazite and xenotime: Mineral stability, REE mobility and fluid composition.
852 *Mineralogy and Petrology*, 99, 165–184.
- 853 Higashimoto, S., Nureki, T., Hara, I., Tsukuda, E., and Nakajima, T. (1983) Geology of the
854 Iwakuni district. Quadrangle Series, Scale 1:50,000, Geological Survey of Japan, 78, 79p.
- 855 Ikeda, T. (1993) Compositional zoning patterns of garnet during prograde metamorphism
856 from the Yanai district, Ryoke metamorphic belt, southwest Japan. *Lithos*, 30, 109–121.
- 857 ——— (1998) Progressive sequence of reactions of the Ryoke metamorphism in the Yanai
858 district, southwest Japan: The formation of cordierite. *Journal of Metamorphic Geology*,
859 16, 39–52.
- 860 ——— (2004) Pressure-temperature conditions of the Ryoke metamorphic rocks in Yanai
861 district, SW Japan. *Contributions to Mineralogy and Petrology*, 146, 577–589.
- 862 Ishihara, S. (1977) The Magnetite-series and Ilmenite-series Granitic Rocks. *Mining Geology*,
863 27, 293–305.
- 864 Janoušek, V., Farrow, C.M., and Erban, V. (2006) Interpretation of whole-rock geochemical
865 data in igneous geochemistry: introducing Geochemical Data Toolkit (GCDkit). *Journal of*
866 *Petrology*, 47, 1255–1259.
- 867 Jefferies, N.L. (1985) The distribution of the rare earth elements within the Carnmenellis
868 pluton, Cornwall. *Mineralogical Magazine*, 49, 495–504.

- 869 Kato, T. (2005) New Accurate Bence-Albee α -Factors for Oxides and Silicates Calculated
870 from the PAP Correction Procedure. *Geostandards and Geoanalytical Research*, 29, 83–
871 94.
- 872 Kawakami, T., and Ikeda, T. (2003) Boron in metapelites controlled by the breakdown of
873 tourmaline and retrograde formation of borosilicates in the Yanai area, Ryoke
874 metamorphic belt, SW Japan. *Contributions to Mineralogy and Petrology*, 145, 131–150.
- 875 Kawano, Y., and Ueda, Y. (1966) K-A dating on the igneous rocks in Japan (V). *The Journal*
876 *of the Japanese Association of Mineralogists, Petrologists and Economic Geologists*, 56,
877 191–211.
- 878 Kelly, N.M., Harley, S.L., and Möller, A. (2012) Complexity in the behavior and
879 recrystallization of monazite during high-T metamorphism and fluid infiltration. *Chemical*
880 *Geology*, 322–323, 192–208.
- 881 Kretz, R. (1983) Symbols of rock-forming minerals. *American Mineralogist*, 68, 277–279.
- 882 Kusiak, M.A., Williams, I.S., Dunkley, D.J., Konečný, P., Šlaby, E., and Martin, H. (2014)
883 Monazite to the rescue: U–Th–Pb dating of the intrusive history of the composite
884 Karkonosze pluton, Bohemian Massif. *Chemical Geology*, 364, 76–92.
- 885 Ludwig, K.R. (2004) Users manual for ISOPLOT/EX, version3.1. A geochronological toolkit
886 for Microsoft Excel. Berkeley Geochronology Center, Special Publication, 4.
- 887 Mielke, P., and Winkler, H.G.F. (1979) Eine bessere Berechnung der Mesonorm für
888 granitische Gesteine. *Neues Jahrbuch für Mineralogie, Monatshefte*, 10, 471–480.
- 889 Montel, J.-M. (1986) Experimental determination of the solubility of Ce-monazite in SiO₂-
890 Al₂O₃-K₂O-Na₂O melts at 800 C, 2 kbar, under H₂O-saturated conditions. *Geology*, 14,
891 659–662.
- 892 Moutte, J., and Iiyama, J.T. (1984) The Ryoke-Sanyo granite series in the Iwakuni-Yanai
893 district, Southwest Honshu, Japan. *Mining Geology*, 34, 425–436.

- 894 Murakami, N. (1971) An example of the emplacement of the Chugoku batholith-the Kuga
895 granites, SW Japan. *Pacific Geology*, 45–56.
- 896 Murata, K.J., Rose Jr, H.J., Carron, M.K., and Glass, J.J. (1957) Systematic variation of rare-
897 earth elements in cerium-earth minerals. *Geochimica et Cosmochimica Acta*, 11, 141–161.
- 898 Nakajima, T. (1994) The Ryoke plutonometamorphic belt: crustal section of the Cretaceous
899 Eurasian continental margin. *LITHOS*, 33, 51–66.
- 900 Nakajima, T., Horie, K., Adachi, T., Miyazaki, K., Dunkley, D.J., and Hokada, T. (2013)
901 SHRIMP U-Pb ages of zircons from Ryoke metamorphic rocks. Geological Society of
902 Japan Annual Meeting, Abstract Volume, 51.
- 903 Nasdala, L. Corfu, F., Blaimauer, D., Chanmuang, C., Ruschel, K., Škoda, R., Wildner, M.,
904 Wirth, R., Zeug, M., and Gamini Zoysa, E. (2017). Neoproterozoic amorphous “ekanite”
905 ($\text{Ca}_2\text{Th}_{0.9}\text{U}_{0.1}\text{Si}_8\text{O}_{20}$) from Okkampitiya, Sri Lanka: A metamict gemstone with excellent
906 lead-retention performance. *Geology*, 45, 919–922.
- 907 Ni, Y., Hughes, J.M., and Mariano, A.N. (1995) Crystal chemistry of the monazite and
908 xenotime structures. *American Mineralogist*, 80, 21–26.
- 909 Nureki, T. (1974) Contact metamorphism in the So-o district, Yamaguchi Prefecture, Japan -
910 With special reference to the occurrence of sillimanite. *Memoirs of the Geological Society*
911 *of Japan*, 11, 251–281.
- 912 Oelkers, E.H., and Poitrasson, F. (2002) An experimental study of the dissolution
913 stoichiometry and rates of a natural monazite as a function of temperature from 50 to 230
914 °C and pH from 1.5 to 10. *Chemical Geology*, 191, 73–87.
- 915 Okudaira, T., Hayasaka, Y., Himeno, O., Watanabe, K., Sakurai, Y., and Ohtomo, Y. (2001)
916 Cooling and inferred exhumation history on the Ryoke metamorphic belt in the Yanai
917 district, South-west Japan: Constraints from Rb-Sr and fission-track ages of gneissose
918 granitoid and numerical modeling. *Island Arc*, 10, 98–115.

- 919 Ondrejka, M., Uher, P., Putiš, M., Broska, I., Bačík, P., Konečný, P. and Schmiedt, I. (2012).
920 Two-stage breakdown of monazite by post-magmatic and metamorphic fluids: An
921 example from the Veporic orthogneiss, Western Carpathians, Slovakia. *Lithos*, 142–143,
922 245–255.
- 923 Pearce, N.J.G., Perkins, W.T., Westgate, J.A., Gorton, M.P., Jackson, S.E., Neal, C.R., and
924 Chenery, S.P. (1997) A Compilation of New and Published Major and Trace Element
925 Data for NIST SRM 610 and NIST SRM 612 Glass Reference Materials. *Geostandards*
926 and *Geoanalytical Research*, 21, 115–144.
- 927 Piechocka, A.M., Gregory, C.J., Zi, J.-W., Sheppard, S., Wingate, M.T.D., and Rasmussen, B.
928 (2017) Monazite trumps zircon: applying SHRIMP U–Pb geochronology to systematically
929 evaluate emplacement ages of leucocratic, low-temperature granites in a complex
930 Precambrian orogen. *Contributions to Mineralogy and Petrology*, 172, 63.
- 931 Poitrasson, F., Chenery, S., and Bland, D.J. (1996) Contrasted monazite hydrothermal
932 alteration mechanisms and their geochemical implications. *Earth and Planetary Science*
933 *Letters*, 145, 79–96.
- 934 Poitrasson, F., Chenery, S., and Shepherd, T.J. (2000) Electron microprobe and LA-ICP-MS
935 study of monazite hydrothermal alteration: Implications for U-Th-Pb geochronology and
936 nuclear ceramics. *Geochimica et Cosmochimica Acta*, 64, 3283–3297.
- 937 Putnis, A. (2002) Mineral replacement reactions: From macroscopic observations to
938 microscopic mechanisms. *Mineralogical Magazine*, 66, 689–708.
- 939 Putnis, A. (2009) Mineral Replacement Reactions. *Reviews in Mineralogy and Geochemistry*,
940 70, 87–124.
- 941 Putnis, A., and Putnis, C.V. (2007) The mechanism of reequilibration of solids in the presence
942 of a fluid phase. *Journal of Solid State Chemistry*, 180, 1783–1786.

- 943 Pyle, J.M., Spear, F.S., Rudnick, R.L., and McDonough, W.F. (2001) Monazite-xenotime-
944 garnet equilibrium in metapelites and a new monazite-garnet thermometer. *Journal of*
945 *Petrology*, 42, 2083–2107.
- 946 Pyle, J.M., Spear, F.S., Wark, D.A., Daniel, C.G., and Storm, L.C. (2005) Contributions to
947 precision and accuracy of monazite microprobe ages. *American Mineralogist*, 90, 547–
948 577.
- 949 Rubatto, D., Müntener, O., Barnhoorn, A., and Gregory, C. (2008) Dissolution-reprecipitation
950 of zircon at low-temperature, high-pressure conditions (Lanzo Massif, Italy). *American*
951 *Mineralogist*, 93, 1519–1529.
- 952 Sato, H. (1933) Yanaizu Geological Map, 1:75 000. Imperial Geological Survey of Japan.
- 953 Scherrer, N.C., Engi, M., Gnos, E., Jakob, V., and Liechti, A. (2000) Monazite analysis; from
954 sample preparation to microprobe age dating and REE quantification. *Schweizerische*
955 *Mineralogische und Petrographische Mitteilungen*, 80, 93–105.
- 956 Schmidt, C., Rickers, K., Bilderback, D.H., and Huang, R. (2007) In situ synchrotron-
957 radiation XRF study of REE phosphate dissolution in aqueous fluids to 800 °C. *Lithos*, 95,
958 87–102.
- 959 Seydoux-Guillaume, A.-M., Paquette, J.-L., Wiedenbeck, M., Montel, J.-M., and Heinrich, W.
960 (2002) Experimental resetting of the U-Th-Pb systems in monazite. *Chemical Geology*,
961 191, 165–181.
- 962 Seydoux-Guillaume, A.-M., Montel, J.-M., Bingen, B., Bosse, V., De Parseval, P., Paquette,
963 J.-L., Janots, E., and Wirth, R. (2012) Low-temperature alteration of monazite: Fluid
964 mediated coupled dissolution–precipitation, irradiation damage, and disturbance of the U–
965 Pb and Th–Pb chronometers. *Chemical Geology*, 330, 140–158.

- 966 Skrzypek, E., Kawakami, T., Hirajima, T., Sakata, S., Hirata, T., and Ikeda, T. (2016)
967 Revisiting the high temperature metamorphic field gradient of the Ryoke Belt (SW Japan):
968 New constraints from the Iwakuni-Yanai area. *Lithos*, 260, 9–27.
- 969 Skrzypek, E., Kato, T., Kawakami, T., Sakata, S., Hattori, K., Hirata, T., and Ikeda, T. (2018)
970 Monazite Behaviour and Time-scale of Metamorphic Processes along a Low-
971 pressure/High-temperature Field Gradient (Ryoke Belt, SW Japan). *Journal of Petrology*,
972 59, 1109–1144.
- 973 Spear, F.S. (2010) Monazite–allanite phase relations in metapelites. *Chemical Geology*, 279,
974 55–62.
- 975 Suzuki, K., and Kato, T. (2008) CHIME dating of monazite, xenotime, zircon and polycrase:
976 protocol, pitfalls and chemical criterion of possibly discordant age data. *Gondwana*
977 *Research*, 14, 569–586.
- 978 Suzuki, K., Adachi, M., and Nureki, T. (1996) CHIME age dating of monazites from
979 metamorphic rocks and granitic rocks of the Ryoke belt in the Iwakuni area, Southwest
980 Japan. *Island Arc*, 5, 43–55.
- 981 Takatsuka, K., Kawakami, T., Skrzypek, E., Sakata, S., Obayashi, H., and Hirata, T. (2018a)
982 Age gap between the intrusion of gneissose granitoids and regional high-temperature
983 metamorphism in the Ryoke belt (Mikawa area), central Japan. *Island Arc*, 27, e12224.
- 984 ——— (2018b) Spatiotemporal evolution of magmatic pulses and regional metamorphism
985 during a Cretaceous flare-up event: Constraints from the Ryoke belt (Mikawa area, central
986 Japan). *Lithos*, 308, 428–445.
- 987 Taylor, M., and Ewing, R.C. (1978) The crystal structures of the ThSiO₄ polymorphs:
988 huttonite and thorite. *Acta Crystallographica Section B*, 34, 1074–1079.
- 989 Taylor, R.J.M., Clark, C., Fitzsimons, I.C.W., Santosh, M., Hand, M., Evans, N., and
990 McDonald, B. (2014) Post-peak, fluid-mediated modification of granulite facies zircon

- 991 and monazite in the Trivandrum Block, southern India. *Contributions to Mineralogy and*
992 *Petrology*, 168, 1–17.
- 993 Terra, O., Dacheux, N., Clavier, N., Podor, R., and Audubert, F. (2008) Preparation of
994 Optimized Uranium and Thorium Bearing Brabantite or Monazite/Brabantite Solid
995 Solutions. *Journal of the American Ceramic Society*, 91, 3673–3682.
- 996 Teufel, S., and Heinrich, W. (1997) Partial resetting of the UPb isotope system in monazite
997 through hydrothermal experiments: An SEM and UPb isotope study. *Chemical Geology*,
998 137, 273–281.
- 999 Tomaschek, F., Kennedy, A.K., Villa, I.M., Lagos, M., and Ballhaus, C. (2003) Zircons from
1000 Syros, Cyclades, Greece—Recrystallization and Mobilization of Zircon During High-
1001 Pressure Metamorphism. *Journal of Petrology*, 44, 1977–2002.
- 1002 Townsend, K.J., Miller, C.F., D’Andrea, J.L., Ayers, J.C., Harrison, T.M., and Coath, C.D.
1003 (2001) Low temperature replacement of monazite in the Ireteba granite, Southern Nevada:
1004 Geochronological implications. *Chemical Geology*, 172, 95–112.
- 1005 Trail, D. (2018) Redox-controlled dissolution of monazite in fluids and implications for phase
1006 stability in the lithosphere. *American Mineralogist*, 103, 453–461.
- 1007 Villa, I.M., and Williams, M.L. (2013) Geochronology of Metasomatic Events. In
1008 *Metasomatism and the Chemical Transformation of Rock* pp. 171–202. Springer Berlin
1009 Heidelberg.
- 1010 Ward, C.D., McArthur, J.M., and Walsh, J.N. (1992) Rare earth element behaviour during
1011 evolution and alteration of the Dartmoor granite, SW England. *Journal of Petrology*, 33,
1012 785–815.
- 1013 Watson, E.B. (1979) Zircon saturation in felsic liquids: experimental results and applications
1014 to trace element geochemistry. *Contributions to Mineralogy and Petrology*, 70, 407–419.

- 1015 Weinberg, R.F., and Hasalová, P. (2015) Water-fluxed melting of the continental crust: A
1016 review. *Lithos*, 212–215, 158–188.
- 1017 Williams, M.L., Jercinovic, M.J., and Terry, M.P. (1999) Age mapping and dating of
1018 monazite on the electron microprobe: deconvoluting multistage tectonic histories.
1019 *Geology*, 27, 1023–1026.
- 1020 Williams, M.L., Jercinovic, M.J., Harlov, D.E., Budzyń, B., and Hetherington, C.J. (2011)
1021 Resetting monazite ages during fluid-related alteration. *Chemical Geology*, 283, 218–225.
- 1022 Yuguchi, T., Sasao, E., Ishibashi, M., and Nishiyama, T. (2015) Hydrothermal chloritization
1023 processes from biotite in the Toki granite, Central Japan: Temporal variations of of the
1024 compositions of hydrothermal fluids associated with chloritization. *American*
1025 *Mineralogist*, 100, 1134–1152.

1026 **FIGURE CAPTIONS**

1027 **FIGURE 1.** Geological map of the Ryoke belt in the Iwakuni-Yanai area (SW Japan), with
1028 sampling localities. Inset shows the area within the Inner Zone of SW Japan (MTL=Median
1029 Tectonic Line). Granitoids are classified according to their emplacement timing relative to the
1030 main, regional tectono-metamorphic event (D1). Lithologies are after Sato (1933),
1031 Higashimoto et al. (1983) and the Geological Survey of Japan (2012). Metamorphic zone
1032 boundaries are after Ikeda (1993). Schist/gneiss boundary modified after Higashimoto et al.
1033 (1983). Mineral abbreviations follow IUGS recommendations after Kretz (1983).

1034 **FIGURE 2.** Microscopic texture of SHK and NAM samples on **(a, b)** EMP scans of thin
1035 sections and **(c, d)** optical microscope photographs. **(a)** Sample SHK showing rounded Qtz
1036 aggregates, Kfs–Pl with straight margins and variably chloritized Bt. **(b)** Sample NAM
1037 showing elongated Qtz layers, aligned Bt and Kfs–Pl with irregular margins. The trace of the
1038 gneissosity is subparallel to the long axis of the thin section. **(c)** Occurrence of Mnz and Aln
1039 in relationship with variably chloritized Bt. SHK, right-hand side of the thin section, plane-

1040 polarized light. **(d)** Ms–Qtz network inside fragmented Kfs, and Mnz grains inside Bt. NAM,
1041 bottom left-hand side of the thin section, crossed polarizers.

1042 **FIGURE 3.** Monazite textures in sample SHK. **(a)** Optical microscope photographs of variably
1043 altered, separated monazite grains. White crosses indicate the location of laser pits. **(b-f)** BSE
1044 images of *in situ* textures and separated grains. **(b)** Euhedral monazite cross-cut by cracks and
1045 surrounded by Ap, Aln, Xtm and a Th–U phase next to chloritized Bt. **(c)** Anhedral monazite
1046 surrounded by zoned allanite, Th–U phase, Xtm and chloritized Bt. **(d)** Oscillatory zoned
1047 allanite protruding into the cleavages of chloritized Bt. Allanite is separated from chlorite by
1048 Al-rich titanite. **(e)** Virtually unaltered monazite with a sector-zoned core and a darker
1049 outermost rim. Limited alteration (darkening) is visible in the bottom right hand part. **(f)**
1050 Altered monazite with Ap, Aln, Xtm, Th–U phase, Chl and Bt present along micro-cracks.
1051 Recrystallization of secondary domains occurred around cracks (darkened parts) and veinlets
1052 (brightened parts). Contrast is adjusted to see the secondary minerals (left) and internal zoning
1053 (right). Same grain as on the right hand photograph in (a).

1054 **FIGURE 4.** Monazite composition in samples from the Shimokuhara (SHK, SHK2) and
1055 Namera (NAM, NAM2) granites. Data are from *in situ* and separated grains. **(a)** REE+Y+P
1056 vs. Th+U+Si diagram (cations for 16 oxygens) highlighting the dominant huttonitic substitution
1057 for primary domain analyses in both samples, and the dominant cheralitic substitution for
1058 secondary domain analyses in NAM. **(b)** Y vs. U diagram (cation fraction on A site) showing
1059 Y–U depletion for some secondary domain analyses in SHK, and Y–U enrichment for
1060 secondary domain analyses in NAM. **(c)** Ternary diagram showing proportions of the
1061 monazite [REEPO₄], “cheralite” [Ca_{0.5}(Th,U)_{0.5}PO₄] and “huttonite” [(Th,U)SiO₄] end-
1062 members for analyses of monazite (all samples) and Th–U phases (SHK & SHK2).

1063 **FIGURE 5.** Monazite textures in sample NAM. **(a)** Optical microscope photographs of
1064 variably altered, separated monazite grains. White crosses indicate the location of laser pits.

1065 **(b-f)** BSE images of *in situ* textures and separated grains. **(b)** Typical mode of occurrence of
1066 monazite inside matrix Bt, with **(c)** an internal structure showing relicts of a sector- or
1067 oscillatory-zoned primary domain cross-cut by a darker secondary domain. **(d)** Virtually
1068 unaltered monazite with a dominant oscillatory-zoned primary domain. A convoluted
1069 secondary domain is slightly developed in the bottom part. **(e)** Altered monazite with a dark
1070 and inclusion-rich secondary domain preferentially developed in the core (included minerals
1071 indicated). Isolated "islands" of primary monazite are left inside the secondary domain. **(f)**
1072 Altered monazite with a dark and inclusion-rich secondary domain developed at the grain
1073 margin (included minerals indicated). The right hand part preserves primary oscillatory
1074 zoning. **(g-h)** Close-up view of rounded and tubular, multi-phase inclusions in monazite.

1075 **FIGURE 6.** Characterization of selected inclusions in secondary monazite domains from
1076 sample NAM. **(a)** Energy dispersion spectra with the most intense element peaks labelled.
1077 The analyzed inclusions are shown in Fig. 5g, h. **(b)** Raman spectra with the shift of the main
1078 vibration bands labelled. The analyzed inclusions are different from those in **(a)**. All spectra
1079 are background-corrected and normalized to the maximum intensity of the most intense
1080 spectrum in each set (vertical intensity scale is arbitrary). The spectra of host monazite are
1081 shown for comparison.

1082 **FIGURE 7.** Results of LA-ICP-MS monazite dating in **(a,b)** sample SHK and **(c,d)** sample
1083 NAM. **(a, c)** BSE images of analyzed monazite grains with representative results. Each spot
1084 location is labelled with spot name, $^{206}\text{Pb}/^{238}\text{U}$ date $\pm 2\sigma$ error (Ma) and concordance (%).
1085 Scale bar is always 20 μm . **(b, d)** Concordia diagrams showing concordant (cc=97–103%)
1086 and discordant (cc < 97% or cc > 103%) analyses for the different monazite domains. Gray-
1087 coded symbols according to U/Th ratio are added in the centre of error ellipses for sample
1088 NAM.

Table 1. Results of mineral mode calculations

	Or	Ab	An	Pl	Qtz	Bt	Chl	Ms	Grt	Ap	Mnz	Ttn*	Hem	Ilm	Crn	Sum	Rest
<i>Mesonorm</i>																	
SHK	17.4	29.5	10.2	39.7	31.8	7.1	-	-	-	0.17	-	-	-	0.21	2.11	98.15	-0.26
NAM	15.3	30.7	8.8	39.6	33.9	6.9	-	-	-	0.24	-	-	-	0.19	2.31	98.22	-0.26
<i>EMP mapping</i>																	
																	ND
SHK	24.7	-	-	30.2	32.7	3.6	4.1	-	0.07	0.05	0.01	0.36	-	-	-	95.71	4.29
NAM	19.1	-	-	38.6	31.2	7.1	-	1.4	0.01	0.05	0.01	-	<i>low</i>	-	-	97.48	2.52

Note: * Titanite mode includes allanite in the case of EMP mapping; *low* =<0.01; ND = no data.

Table 2. Representative analyses of monazite domains and Th-U phase

Sample	SHK				NAM	
	99a-m41	99a-m34	99a-Mnz9	99a-Ac2	117a-m35	117a-Mnz17
Spot	primary core	primary rim	secondary	Th-U phase	primary	secondary
<i>Wt% oxides</i>						
SiO ₂	2.30	0.60	0.63	18.16	0.70	0.44
P ₂ O ₅	27.31	29.70	29.39	0.78	29.63	29.29
CaO	1.08	0.83	0.11	1.26	0.86	1.30
ThO ₂	14.62	5.89	2.69	62.77	6.88	6.84
UO ₂	0.73	0.45	d.l.	5.64	0.15	0.45
Y ₂ O ₃	2.53	3.22	0.74	1.10	0.65	1.46
La ₂ O ₃	11.35	13.31	12.80	0.195	16.90	11.50
Ce ₂ O ₃	22.28	26.60	30.06	0.32	29.77	26.58
Pr ₂ O ₃	2.53	2.82	3.72	d.l.	2.92	3.14
Nd ₂ O ₃	10.88	11.08	13.41	0.34	10.56	11.49
Sm ₂ O ₃	2.28	2.51	3.45	d.l.	1.27	3.19
Gd ₂ O ₃	2.09	2.30	2.43	0.35	0.70	2.01
Tb ₂ O ₃	n.a.	n.a.	0.19	n.a.	n.a.	0.19
Dy ₂ O ₃	n.a.	n.a.	0.57	n.a.	n.a.	0.61
Ho ₂ O ₃	n.a.	n.a.	d.l.	n.a.	n.a.	d.l.
Er ₂ O ₃	n.a.	n.a.	d.l.	n.a.	n.a.	0.14
Tm ₂ O ₃	n.a.	n.a.	0.34	n.a.	n.a.	0.29
Yb ₂ O ₃	n.a.	n.a.	d.l.	n.a.	n.a.	d.l.
PbO	0.04	0.02	d.l.	0.198	d.l.	0.02
Total	99.98	99.34	100.53	91.12	100.97	98.92
<i>Cations</i>						
Si	0.366	0.094	0.099	0.988	0.109	0.069
P	3.681	3.932	3.912	0.036	3.908	3.934
Ca	0.184	0.138	0.018	0.073	0.143	0.221
Th	0.530	0.210	0.096	0.777	0.244	0.247
U	0.026	0.016	0.000	0.068	0.005	0.016
Y	0.214	0.268	0.062	0.032	0.053	0.123
La	0.667	0.768	0.742	0.004	0.971	0.673
Ce	1.299	1.523	1.730	0.006	1.698	1.544
Pr	0.147	0.161	0.213	-	0.166	0.182
Nd	0.619	0.619	0.753	0.007	0.588	0.651
Sm	0.125	0.135	0.187	-	0.068	0.174
Gd	0.110	0.119	0.127	0.006	0.036	0.106
Tb	-	-	0.010	-	-	0.010
Dy	-	-	0.029	-	-	0.031
Ho	-	-	-	-	-	-
Er	-	-	-	-	-	0.007
Tm	-	-	0.017	-	-	0.014
Yb	-	-	-	-	-	-
Pb	0.001	0.001	-	0.003	-	0.001
Total	7.968	7.985	7.995	2.000	7.990	8.003
<i>X_{mz}</i>	0.811	0.908	0.971	0.059	0.901	0.879
<i>X_{cher}</i>	0.094	0.070	0.009	0.150	0.072	0.110
<i>X_{hut}</i>	0.095	0.022	0.020	0.792	0.027	0.011
T (°C) ^a	-	-	482	-	-	533
T (°C) ^b	-	-	572	-	-	618

Notes: n.a. = not analyzed; d.l. = below detection limit

Monazite: cations normalized to 32 charges; Th-U phase: normalization to 2 cations

^aCalibration after Pyle et al. (2001)

^bCalibration after Heinrich et al. (1997)

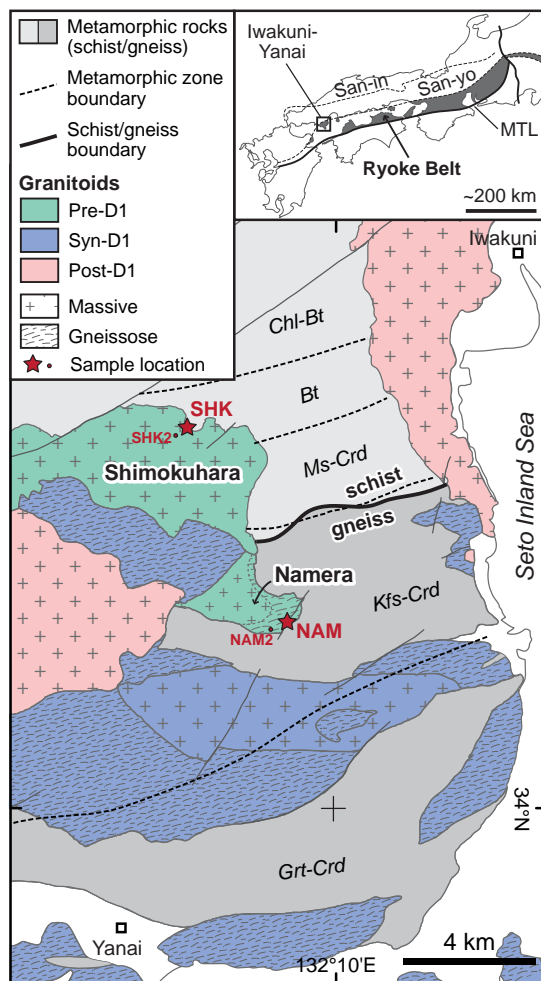
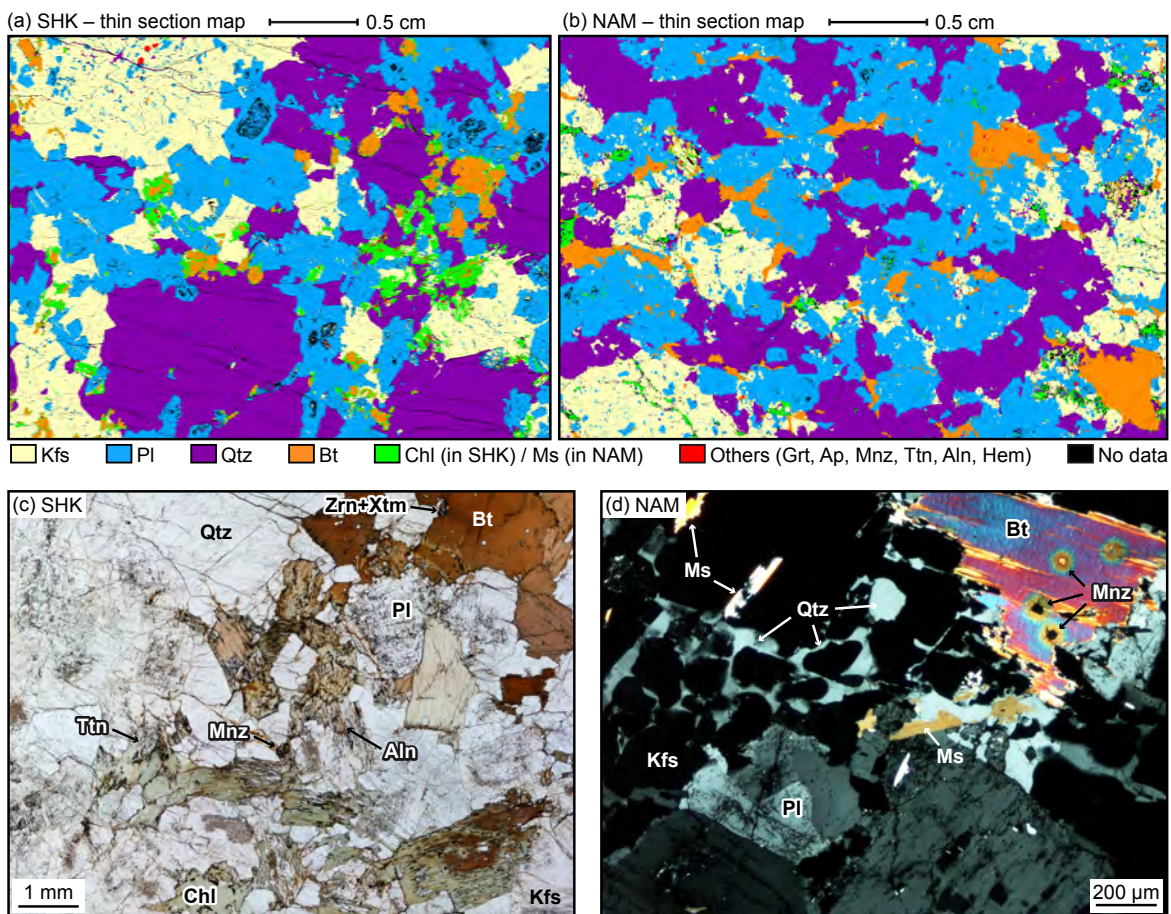


Figure 1



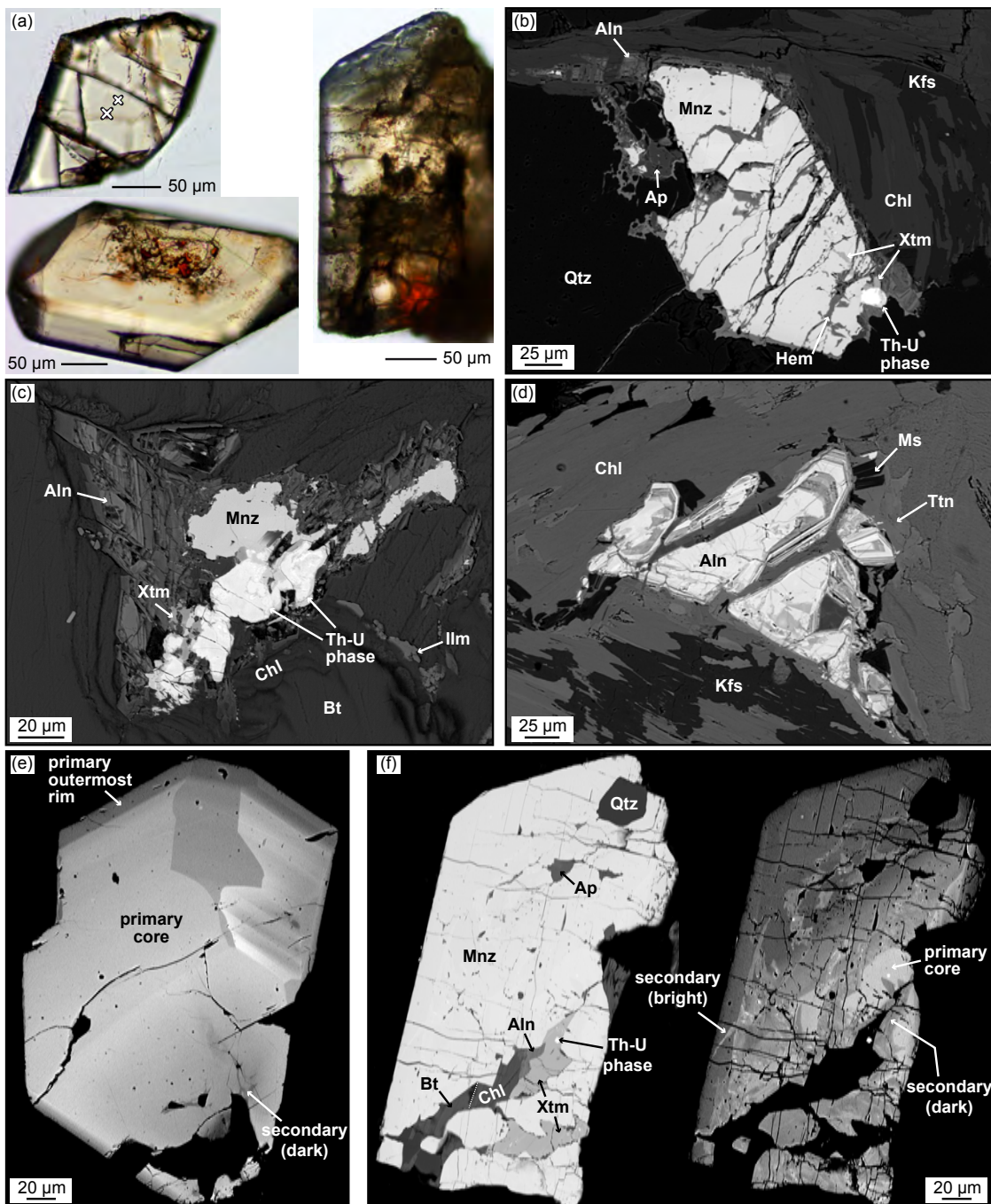


Figure 3

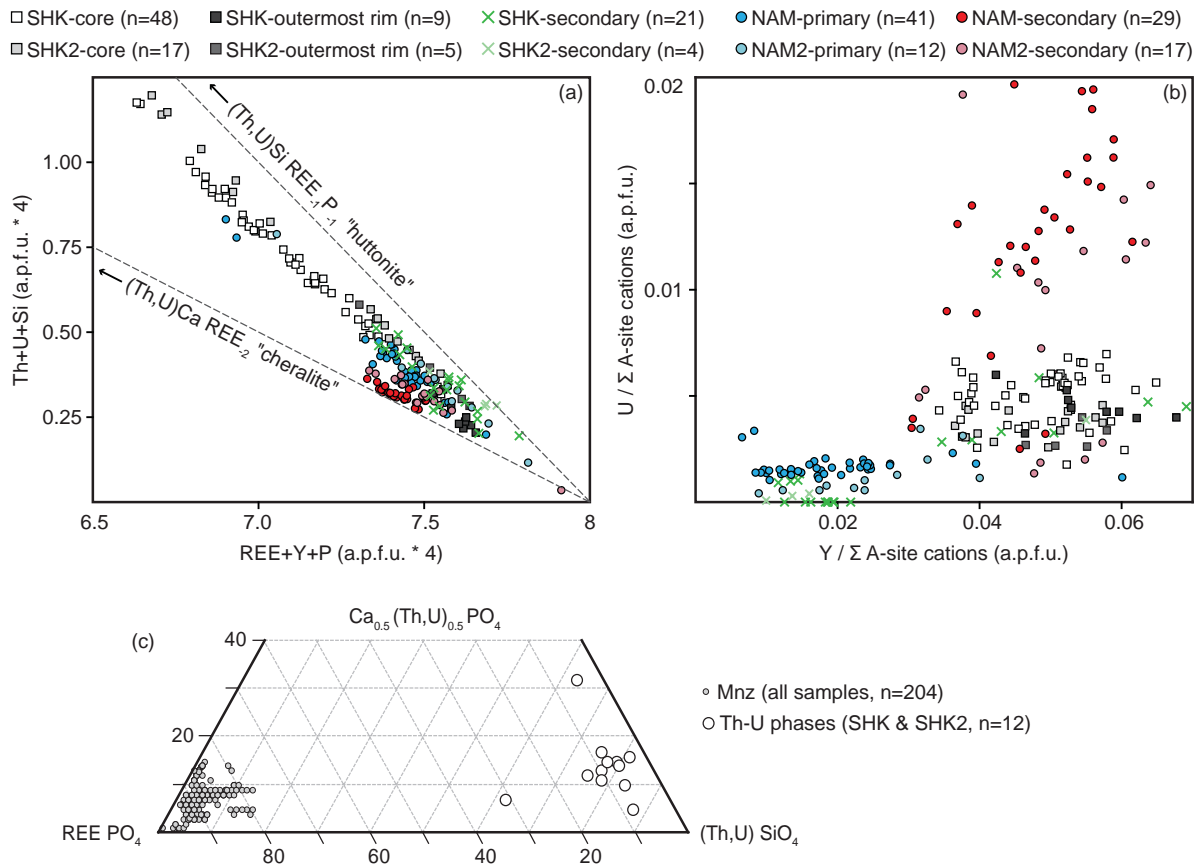
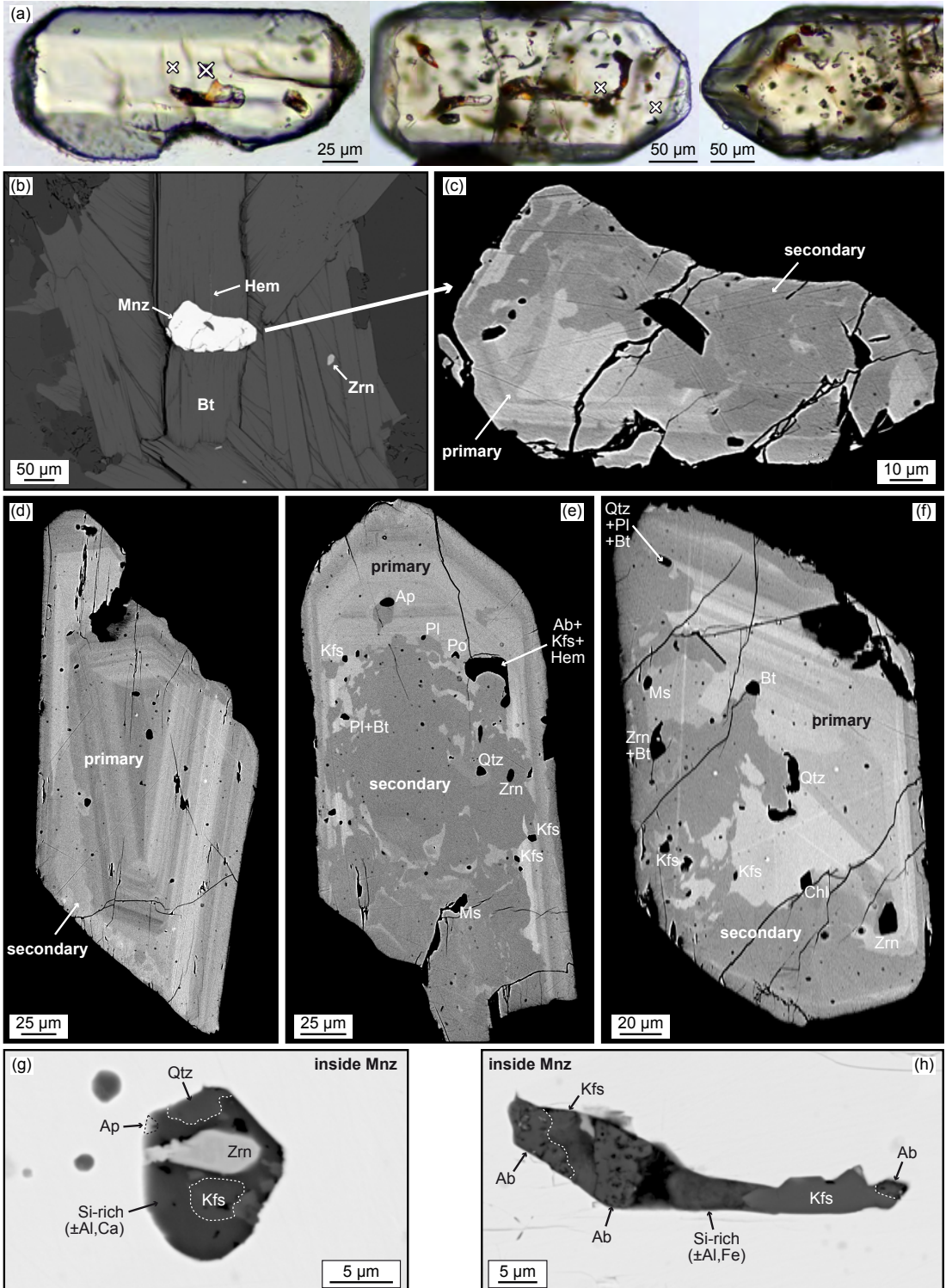


Figure 4



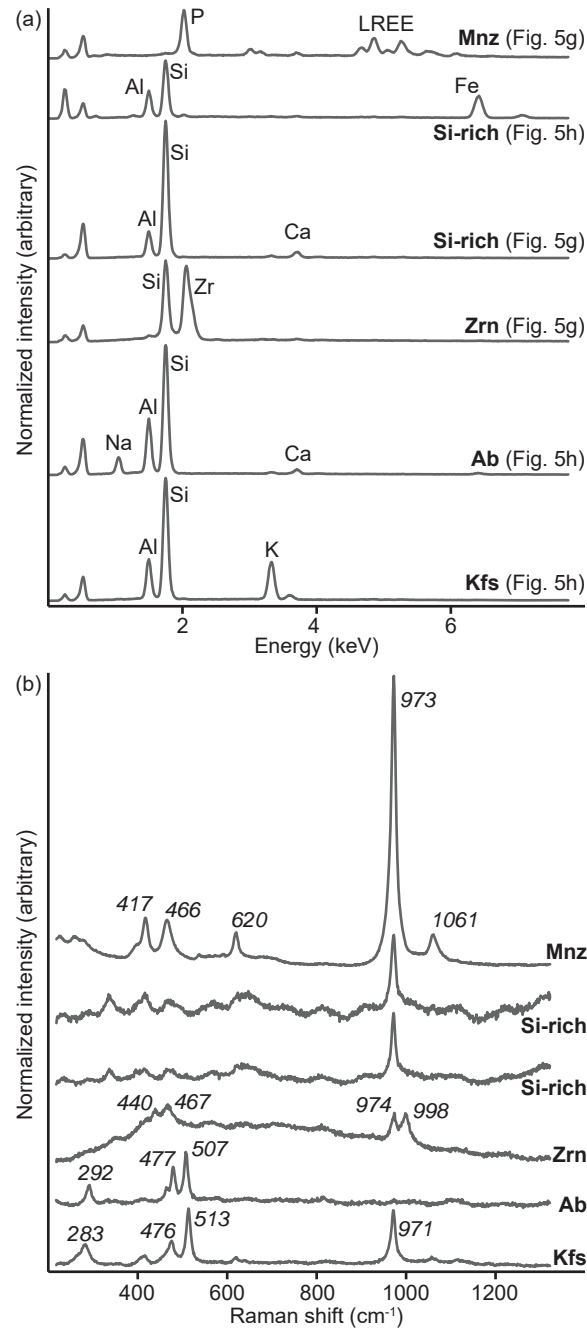


Figure 6

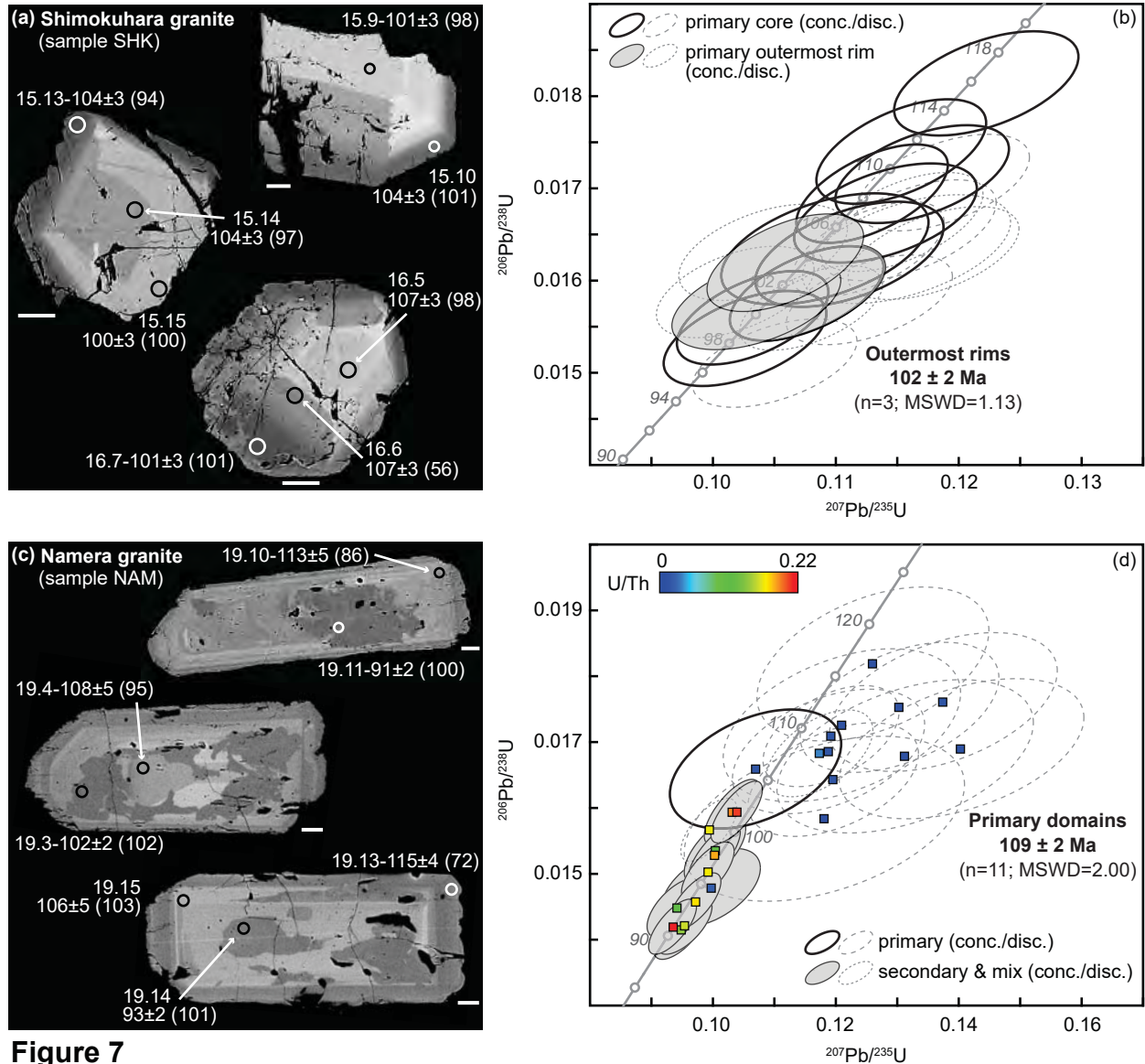


Figure 7